RESEARCH ARTICLE

I. Cosadia · J. Borée · G. Charnay · P. Dumont

Cyclic variations of the swirling flow in a Diesel transparent engine

Abstract PIV data obtained in a transparent motored
Diesel engine are presented and discussed in this paper.
These data are obtained in severe thermodynamical
conditions in the cylinder during the cycle and in the
bowl at top dead center (TDC). Moreover, they are
obtained at consecutive cycles. We first consider the flow
in the middle of the compression phase. In particular,
instantaneous velocity fields are analyzed and classified
by computing circulation statistics. We show that the
structure of the swirling motion is varying very signifi-
cantly from "vortex type" to "annular type" from one
cycle to another. In-cycle and inter-cycle statistics of
these structure fluctuations are discussed. For example,
we do not find any cycle-to-cycle correlation. The cir-
culation data are then decomposed by using a proper
orthogonal decomposition of the statistical set. The
possibility of low order description of this kind of flow is
considered. Finally, we study the in-bowl flow at the
very end of the compression phase. The quantitative
analysis based on circulation statistics show that we still
detect strong structure fluctuations of the swirling flow
at TDC and that the intensity of these fluctuations have
not decreased after the squish phase.

I. Cosadia (✉) · P. Dumont
RENAULT s.a.s., Aérodynamique & Nouveaux Concepts,
1 Allée Cornuel, 91510 Lardy, France
E-mail: imran.cosadia@renault.com

J. Borée
Laboratoire d'Etudes Aérodynamiques, LEA-ENSMA UMR
CNRS 6609, Téléport 2, 1 avenue Clément Ader,
BP 40109, 86961 Futuroscope Chasseneuil, France

G. Charnay
Institut de Mécanique des Fluides de Toulouse,
IMFT UMR CNRS/INPT 5502, Allée du Professeur Camille
Soula, 31400 Toulouse, France

1 Introduction

Charge motion within diesel cylinder is known to be of
important interest. Indeed, the air motion critically af-
fects the combustion quality (Heywood 1988; Payri et al.
1996) and pollutant emissions. A specific mean flow,
called "swirl" is induced in the cylinder. The charge
rotates around an axis parallel to the cylinder axis and
evolves under the piston displacement. The idea behind
the swirl induction is to encapsulate some of the
momentum of the inlet valve air jet in a large rotating
coherent motion, which is less dissipative than turbu-
lence and hence will retain energy longer. To quantify
this swirling motion, researchers have proposed many
definitions (Reuss et al. 1989; Crnojevic et al. 1999). The
quantities obtained were most of the time based on the
solid-body rotation hypothesis or on homogeneous
motion within the cylinder.

To comply with severe pollution—reduction
requirements, the large-scale rotating air motion is
introduced into the combustion chamber so that the fuel
spray is correctly mixed during the injection process.
The angular momentum of this induced air motion must
be large enough to ensure good transport properties but
not so large that spray plumes overlap. Indeed, the
combustion process will mainly depend on the spray
characteristics and also on its interaction with the air
motion in the chamber. These features have to be the
same from one cycle to the other. Unfortunately, cyclic
variations occur most of the time in the combustion
chamber (Enotiadis et al. 1990). There exist therefore
differences between consecutive or non-consecutive cy-
cles, which are harmful to the combustion. Thus, even if
it has been argued that the energetic, penetrating fuel
spray and the simultaneous multi-point ignition process
in Diesel engines integrate or average over details of the
in-cylinder flow, engine design must take into consider-
ation the flow large-scale fields' repeatability, since this
obviously will affect efficiency and emissions. The mixing
process will also be strongly influenced by the turbulence

features of the flow, i.e. small-scale motions, which are responsible for species diffusion. The knowledge of the bulk motion in the cylinder and of the turbulence evolution is thus of great importance for the improvement of engines.

Even if the importance of in-cylinder flow was recognized quite early, one had to wait for the development of optical diagnostic techniques and especially for laser Doppler velocimetry (LDV) to obtain detailed measurements in combustion chambers (Arcoumanis and Whitelaw 1987; Arcoumanis et al. 1983, 1987, 1991; Hill and Zhang 1994; Payri et al. 1996). Local measurements of one or two components of the velocity fields are most often obtained in chosen points and provide useful information about the structure of the flow (Gerber et al. 1981, 1985) and the state of turbulence. For instance, phenomena such as swirl–squish interaction in a typical diesel bowl-in piston have been investigated in the early work of (Arcoumanis et al. 1983).

It is, however, very difficult to understand the instantaneous spatial structure of the flow from these data. Visualization tools and optical methods were then adapted and used to solve complex flows and to allow a better understanding of the physical process implied.

Particle image velocimetry (PIV) is such a complementary technique. PIV of in-cylinder flow was pioneered by (Reuss et al. 1989). Spatial filtering was used in these early works to distinguish between large-scale and small-scale features. PIV provides a clearer description of the structure of the flow field in transparent research engines. It is becoming now an efficient investigation tool in the industry (Baby 2000). Most of the time, PIV has been applied on gasoline engine. Due to thermodynamical and geometrical constraints, it was difficult to apply such techniques to Diesel engines which have a high compression ratio. Many efforts have been made to overcome those issues and we present in this work PIV results obtained from one transparent Diesel engine.

It is now well established that the assumption of a solid body swirling flow in an engine with a piston is an oversimplification. For example, the recent observations (Towers et al. 2004) showed that the swirling flow in a model GDI engine is far from having a solid rotation velocity distribution. Moreover, spatial inhomogeneities have also been observed in a Diesel engine with bowl-in piston by Deslandes et al. (2004). Thus, the large amount of information gained during those last decades in in-cylinder aerodynamics through LDV are being under reconsideration since the need for new structure quantification tools is becoming a crucial preoccupation.

The research engine from which we got the results presented here has been built by RENAULT s.a.s. in order to improve the understanding of the flow structure and the cyclic variations of the swirling flow. Our objectives here are two-fold:

1. To focus our analysis on the middle of the compression phase, at $\theta = 270$ CAD (crank angle degree) by using the PIV data in order to illustrate the structure of the flow. We will particularly emphasize the repeatability and structure of the swirling flow by computing circulation statistics.
2. To take advantage of the present set up to obtain reliable data in the bowl even at TDC (top-dead center), and at consecutive cycles. These data at TDC will be analyzed in order to see if the intensive transfer of mass (squish) occurring at the very end of the compression has an effect on the repeatability and structure of the swirling flow. This provides a better understanding of the in-cylinder flow prior to fuel injection.

The fluctuations that occur during air induction and compression strokes are responsible for a high variability of the flow patterns. Reynolds Averaged Navier–Stokes (RANS) decomposition used in most of the industrial computational fluid dynamics (CFD) codes is unable to detect those kinds of large scale variability. This default is definitely linked with the phase averaging procedure associated with the Reynolds statistical approach. To overcome this limitation, other kinds of decompositions can be used (see e.g. Bonnet et al. 2002). The main objective is then to propose an alternative way to Reynolds statistical decomposition and to extract from the velocity field some coherent features which may provide a description of the large-scale motions variability of the swirling flow. By this way, cyclic variability might be formally identified and control strategies might be proposed.

In the context of analyzing the statistical properties of the swirl, proper orthogonal decomposition (POD) is thus applied to our dataset. The POD was proposed in (Lumley 1967) to extract coherent structures from turbulent flows. This method is unbiased since the decomposition functions are not of pre-determined form, but constructed through an optimization process. It is optimal as far as the kinetic energy contained in the successive modes is concerned. This statistical tool is now widely applied for analyzing experimental data obtained with PIV or rakes of hot wires. It can also be useful for extracting relevant information from the large amount of data obtained with direct numerical simulation (DNS) or large eddy simulation (LES). When most kinetic energy in the flow domain analyzed by the POD is embedded in a large-scale rotating structure, a common result is that low-order modes are associated with temporal and cyclic variation of the structure. In a well-defined rotating flow, (Graftieaux et al. 2001) has shown that three modes are sufficient to characterize the vortex wandering. Although there is no really clear separation in the POD energy spectrum in Diesel applications, extensive tests have shown that POD could be a practical way to extract large-scale cycle-to-cycle fluctuations from the data sets. This will be applied to statistics of the velocity circulation and introduced as a way to quantify structure variability in the present flow.

2 Experimental setup and measurements

2.1 Experimental configuration

A model optical Diesel engine with a common four-valve cylinder head, and with two directional intake pipes, was used in this study. The whole description of the test bench is beyond the scope of the paper. Engine features have been summarized in Table 1.

Experimental set-up is a motored four-valve single-cylinder engine with plate roof combustion chamber which allows different compression ratio (from 12 to 21). The engine rotation speed has been fixed at 1,200 rpm during all the experiments. Except for the piston shape, which is cylindrical, the single-cylinder engine has got the same features as a real engine. The quartz cylinder is completely transparent. PIV measurements through transparent piston with a real shape are critical since optical distortions are very strong and cannot be easily corrected. This is why we used a simplified piston shape. Since diesel thermodynamic conditions are higher than spark ignition engine, developing new technologies concerning piston management appeared as a necessity. Piston rings with no lubrication permit to keep a correct pressure inside cylinder without scratching glasses. Ring material must be heatproof since the in-cylinder temperature is up to 500°C. Its low coefficient of thermal expansion avoids engine jamming and ensures a low blow-by. Instead of a mechanical fixation for the transparent piston, a technology using glue developed specially by Renault s.a.s. was used. This sticking-based technology allows a large visualization area in the cylinder and it also allows visualization in bowl from all sides. For the horizontal measurement planes, which are perpendicular to the cylinder axis, images are recorded via a mirror placed under the piston.

Five horizontal measurement planes have been chosen at $\theta = 270$ CAD. These planes fit the bulk of an entire quartz cylinder diameter, as presented in Fig. 1. At the end of compression phase, at $\theta = 360$ CAD, three planes have been used to quantify the aerodynamical fields within the bowl-in piston (Fig. 2).

For the vertical measurement planes (parallel to the cylinder axis), difficulties raised in obtaining measurements when the light sheet is not in the symmetry plane. Indeed, laser illumination then results in very strong reflections. However, considerable efforts have been undertaken to overcome this difficulty, all the more so as

Table 1 Engine dimensions and characteristics

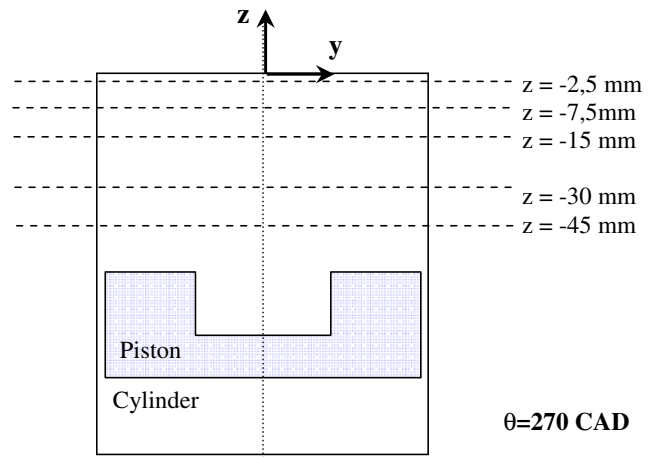| Bore b	80 mm	Bowl depth	15 mm
Stroke S	93 mm	Squish height	0.7 mm
Engine speed	1,200 rpm	Maximum temperature at TDC	550°C
Bowl diameter d_b	38 mm	Maximum pressure at TDC	40 bars
Cylinder head	4-valve	Compression ratio	20

Fig. 1 Horizontal measurement planes for $\theta = 270$ CAD. The distance between the roof and the piston crown is about 55 mm
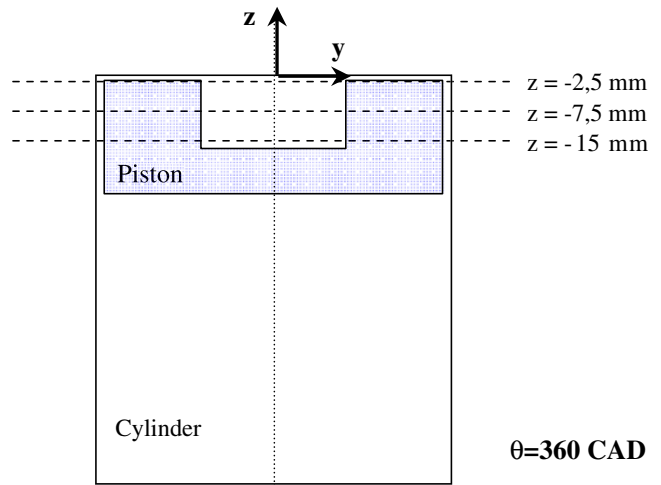

Fig. 2 Horizontal measurement planes for $\theta = 360$ CAD. The distance between the roof and the piston crown is about 0.7 mm
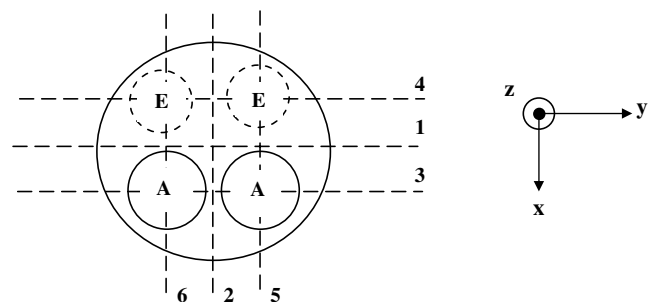

Fig. 3 Vertical measurement planes. *A* Inlet valves. *E* Exhaust valves. Measurements were performed for both $\theta = 270$ CAD and $\theta = 360$ CAD

the knowledge of the flow patterns in those planes is essential. Six vertical measurement planes are available (Fig. 3).

2.2 Visualization system

The PIV system consists in a double pulsed Nd: Yag laser, which light sheet was adjusted to 1 mm. The laser frequency is 10 Hz. Acquisition was carried out by a 1008×1018 pixels-size CCD camera. As all the CCD was being imaged, the PIV image fields are about 100×100 mm^2 for both horizontal and vertical measurement planes.

For all the measurements, the velocity vectors computation conditions were fixed. Adaptive inter-correlation (DANTEC Correlator ®) has been processed on 32×32 pixels-size final interrogation spots, with 50% overlap, which gives a 62×62 vectors grid. True size (without overlap) of the interrogation windows is $\Delta \approx 2.5$ mm. Particle images treatment consists in using subpixel cell shifting and deformation, allowing bias and random error reduction (Lecordier 1997). A widely accepted estimation of the absolute displacement error using these algorithms is 0.05 pixels.

Different thresholds including signal-to-noise ratio (minimal value of 1.21) and velocity vector magnitude were used as post-processing steps. Residual spurious vectors have been detected using a comparison with the local median of a 7×7 neighborhood for each grid points (Westerweel 1993). The number of spurious vectors was always low (less than 1% of the whole vectors field). No further filtering has been applied to the velocity fields in order to keep the whole measurement information.

Optical deformations are linked to optical access. The horizontal measurement planes are recorded through a cylindrical piston, which is a simplified shape compared to those commonly used in real engine piston configuration. Spherical aberration, field aberration and distortion have been estimated to give the particle position error. The effects of these optical aberrations were weak compared to the particle size. They were consequently not corrected, since they do not significantly affect the results. The cylinder shape also entails optical deformations in the vertical measurement planes. Since the PIV velocity fields discussed in this work are mainly obtained in horizontal planes and because we are interested in the bulk flow, the vertical velocity fields presented in Fig. 5a–d are not corrected for image distortion due to the cylinder shape.

Synchronization with engine angular information and operation frequencies allowed having one measurement, i.e. one instantaneous velocity field, at every engine cycle. This is particularly useful to point out cyclic variations of the flow.

In the following, vectors will be denoted in bold. The reference frame was set so as **z** is the ascendant axis and **x** is the axis between the two intake ports (Fig. 3). In the vertical PIV fields, the origin is chosen in the middle of the cylinder head. In the horizontal fields, it was chosen in the middle of the cylinder and corresponds to $(x, y) = (0, 0)$. U, V and W are the velocity component along, respectively, x, y and z axis. The sets analyzed are composed of 300 double-pictures at a given phase (270

CAD or 360 CAD) during the compression stroke. The symbol $\langle \ \rangle$ indicates phase averaging operator. Unless specified, the components of the instantaneous fluctuating velocity field are denoted, respectively, by (u, v, w). POD modes will be computed in the frame of the method of snapshots introduced in (Sirovich 1987)—see also (Berkooz et al.1993) for more details. We appreciate that $M = 300$ fields per phase is a rather small number to perform a quantitative POD analysis. Nevertheless, we maintain that the results illustrate very clearly the properties of the swirling motion.

2.3 Seeding constraints

Applying PIV in a Diesel engine also entails strong constraints on seeding material. Solid particles were used to avoid burning the flow tracers. However, finding a solid material that could be introduced in the cylinder without damaging the quartz window and the piston rings was time consuming. The time response of the flow tracers used here in air at standard conditions (Atmospheric pressure, temperature equal to 20°C) is $\tau_p = \rho_p d_p^2/18\mu_a = 3.5\times 10^{-4}s$. ρ_p is the density of the beads, d_p their diameter. μ_a is the air viscosity. Note that μ_a is increasing during the compression stroke (the viscosity of the air globally evolves like the square root of the temperature inside the chamber, according to Sutherland's law). Consequently, the time response of the particles is decreasing between the bottom and the top dead center as indicated in Table 2. Four time scales have been compared to τ_p in order to evaluate the seeding quality for this engine flow:

1. $\tau_e = S/\bar{V}_p$ is the engine time scale. S is the piston stroke and $\bar{V}_p$ is the mean speed of the piston. τ_e characterizes the rate of the flow variation imposed by the time varying boundary conditions. τ_e is indicated in Table 2. We see that $\tau_p \ll \tau_e$. Seeding particles are therefore able to follow these changes.

2. $\tau_S = 1/\omega_S$ is the mean swirl turn-over time scale. ω_S is an equivalent rotation rate computed classically as $\omega_S = N_S.\omega$ where N_S is the swirl number and ω the rotation rate of the engine. At TDC, ω_S increases and can be estimated by assuming that the mean angular momentum of the flow is a constant. We see

Table 2 Particles and flow time scales according to the CAD

	$\theta = 180$ CAD	$\theta = 270$ CAD	$\theta = 360$ CAD
τ_p(s)	3.5×10^{-4}	3.5×10^{-4}	1.5×10^{-4}
τ_e(s)	2.5×10^{-2}	2.5×10^{-2}	2.5×10^{-2}
τ_S(s)	4.0×10^{-3}	4.0×10^{-3}	1.0×10^{-3}
τ_t(s)	3.6×10^{-3}	3.6×10^{-3}	1.3×10^{-3}
τ_Δ(s)	1.2×10^{-3}	1.9×10^{-3}	

τ_p time response of the flow tracers; τ_e engine time scale;$\tau_S$mean swirl turn-over time scale; τ_t turbulent turn-over time scale;τ_Δ turn-over time scale of small eddies of the size Δ of the PIV interrogation window

$(<\mathbf{V}>,<\mathbf{U}>) \quad \rightarrow 10 \text{ m.s}^{-1}$

a

$(<\mathbf{V}>,<\mathbf{U}>) \quad \rightarrow 10 \text{ m.s}^{-1}$

b

$(<\mathbf{V}>,<\mathbf{U}>) \quad \rightarrow 10 \text{ m.s}^{-1}$

c

$(<\mathbf{V}>,<\mathbf{U}>) \quad \rightarrow 10 \text{ m.s}^{-1}$

d

$(<\mathbf{V}>,<\mathbf{U}>) \quad \rightarrow 10 \text{ m.s}^{-1}$

e
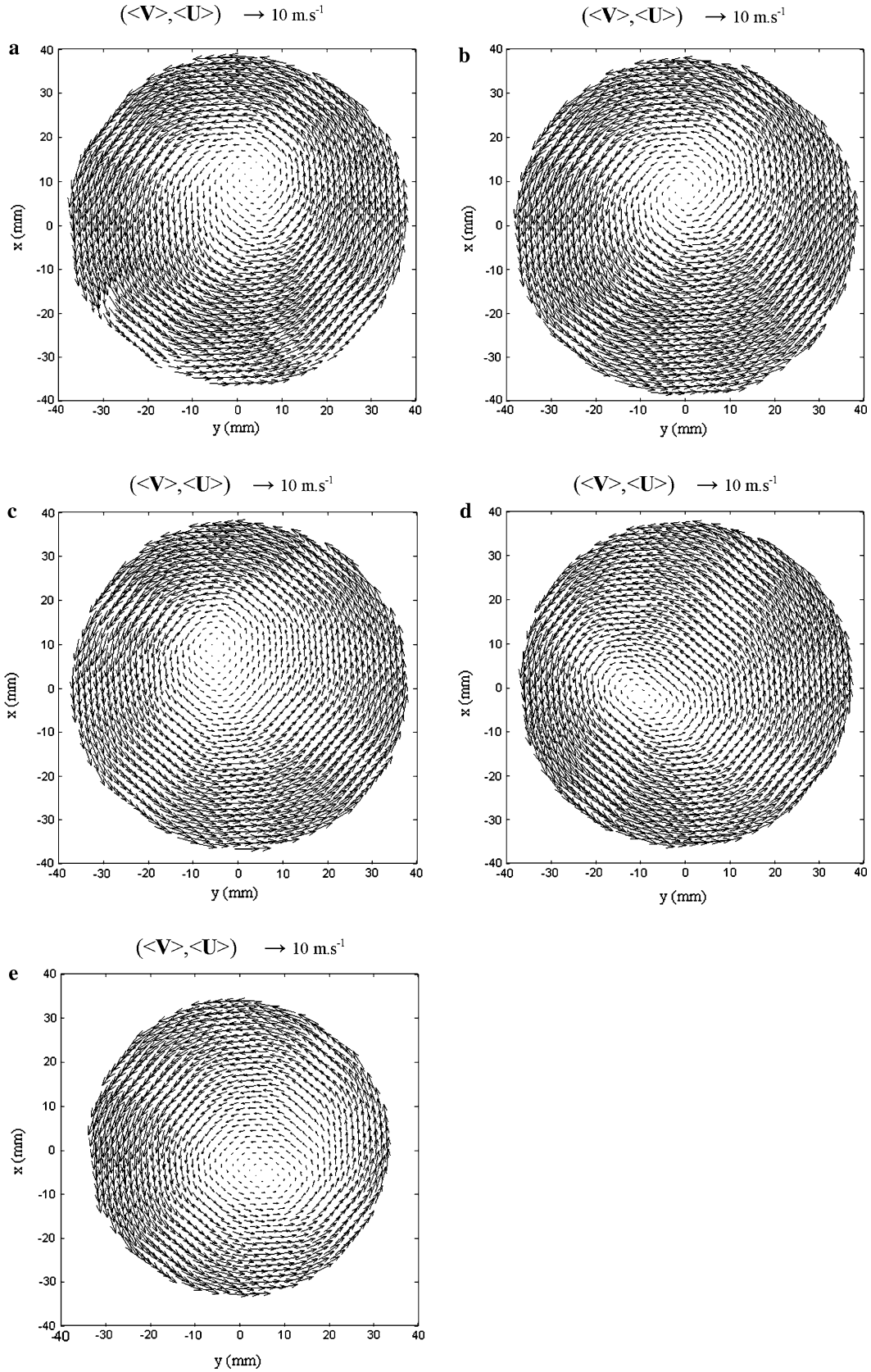
Fig. 4 Phase-averaged mean velocity fields for each measurement plane, for $\theta = 270$ CAD: **a** $z = -2.5$ mm; **b** $z = -7.5$ mm; **c** $z = -15$ mm; **d** $z = -30$ mm; **e** $z = -45$ mm

in Table 2 that the particles are able to follow accurately the large scale swirling motion.

3. $\tau_t = L/u'$ is the turbulent turn-over time scale. L is the size of the energy containing eddies and u' is an order of magnitude of the rms velocity associated to these eddies. We are interested here in the global properties of the turbulent flow in the combustion chamber. Following Lumley (1999), we have therefore chosen the following estimates: $(\theta, L, u') = (180°, b/6, \bar{V}_\mathrm{p})$; $(270°, b/6, \bar{V}_\mathrm{p}/2)$; $(360°, p/6, \bar{V}_\mathrm{p}/2)$. b is the cylinder bore, p is the depth of the bowl and $\bar{V}_\mathrm{p}$ is the mean piston speed. τ_t is indicated in Table 2 at these three phases. A Stokes number $S_t = \tau_\mathrm{p}/\tau_t$ can be computed and is of the order of 1/10. The particles are able to follow the large scale fluctuations of the turbulent velocity field.

4. $\tau_\Delta = \tau_t\,(\Delta/L\,)^{2/3}$ is the turn-over time scale of small eddies of the size Δ of the PIV interrogation window. $\Delta \approx 2.5$ mm is obviously the smallest turbulent scale that can be detected by the PIV measurements. In Table 2, τ_Δ was estimated at $\theta = 180, 270$ CAD only because this estimation is valid if the eddies of size Δ belong to the inertial scales (Tennekes and Lumley 1972). The Stokes number $S_{t\Delta} = \tau_\mathrm{p}/\tau_\Delta$ is of the order of $S_{t\Delta} \approx 0.3$. Moreover, $(\Delta/L) \approx 1/5$ at $\theta = 180, 270$ CAD and $(\Delta/L) \approx 2/5$ at $\theta = 360$ CAD. This means that the spatial filtering induced by PIV and the temporal filtering due to the particles prevent an accurate resolution of the turbulence spectrum in these measurements. For example, for $(\Delta/L) \approx 1/5$, and if scale Δ belong to the inertial subrange, the ratio between the kinetic energy carried by large scales and by scales Δ is $u^2\,(\Delta)/u^2(L) \approx [\Delta/L\,]^{2/3} \approx 34\%$. This is not a real problem for this study because we will focus on the large scale variability of the flow by introducing integral properties.

3 Analysis of the middle compression phase

3.1 Phase-averaged velocity fields

The ensemble-averaged velocity fields for each plane are presented in Fig. 4a–e. For clarity reasons, only one out of two velocity vectors are plotted. The highest magnitude observed in the chamber is $U_m \approx 12$ m/s, which is quite a high level in this small domain. The flow is effectively a "swirl" and it exhibits a zero-velocity point, which is not located at the geometrical center of the cylinder $(x, y) = (0, 0)$. Moreover, the location of the zero-velocity point is different from one plane to another, revealing deformations and inhomogeneities in the mean velocity distribution. One might be tempted to consider the zero-mean velocity point as the center of a coherent vortex. However, we will show in the following that the structure of the instantaneous flow is more complex and cannot be reduced to a single large scale vortex. The main direction of the flow is given to be azimuthal, as expected by the engine inlet ports architecture. Nevertheless, the non-axisymmetrical aspect of the mean air motion is clear. This implies a non-rigid-body like rotation while the rigid-body hypothesis is often taken to calculate air rotation as a solid disk rotation (total angular momentum divided by inertia). Moreover, this swirling motion quantification is computed relative to the center of the chamber, which is shifted from the zero-mean velocity point.

The phase averaged velocity fields in the vertical symmetry plane "2" and in the lateral plane "5" located under the valves (see Fig. 3) are presented in Fig. 5a, b. Data in other lateral planes are available but not presented here for brevity. For a deterministic pure solid body rotation strictly centered on the axis of the cylinder and compressed by the motion of the piston, we would measure a pure vertical velocity in the symmetry plane. The charge rotation would be detected in the lateral plane but it is easy to check out that the angle $\alpha = \mathrm{Arctg}(W/U)$ in such plane should be a function of z only, decreasing when one moves toward the roof of the chamber. Such simple velocity fields are clearly not observed in Fig. 5a, b. The structure of the flow is more complex. In particular, we detect quite large mean vertical velocities (of the order of 6 m/s, i.e. half of the maximum mean azimuthal velocity) in the central region of the chamber (Fig. 5a). This corresponds to the core region of the swirling flow that will be considered in the following.

At $\theta = 270$ CAD, the volume of the bowl is only 6% of the in-cylinder volume. Making the assumption of a pure vertical flow driven by the motion of a flat piston, we easily obtain the mean vertical velocity component $\langle W \rangle$ as:

$$\langle W \rangle = \langle W_0 \rangle + \langle W_1 \rangle \tag{1}$$

$\langle W_0 \rangle$ is the mean solenoidal velocity component and $\langle W_1 \rangle$ is the mean velocity component induced by the dilatation rate (Batchelor 1967). Neglecting the influence of the bowl, the vertical velocity component $\langle W_0 \rangle$ can then be expressed as:

$$\langle W_0 \rangle = \langle W \rangle - \frac{V_\mathrm{p}}{z_\mathrm{p}}z, \tag{2}$$

where V_p in the instantaneous piston speed and z_p the position of the piston crown. The spatial average of $\langle W_0 \rangle$ computed by using the five vertical measurement planes is $\langle \tilde{W}_0 \rangle \approx 1,3\,m/s$. $\tilde{W}_0$ is much smaller than U_m and this is the reason why we will focus on horizontal planes in the following. However, considering (a) the large scale variability of the swirling motion discussed next, (b) the fact that high vertical velocities can "burst" in the core of the swirling motion, we see clearly that stereo-PIV data obtained in the vertical symmetry plane would be of great interest. This is the subject of ongoing developments. The mean solenoidal velocity field $\langle W_0 \rangle$ is drawn in Fig. 5c, d. The bowl is of course not under consideration in Fig. 5c. We detect a weak tumbling

component in Fig. 5d. The solenoidal field is less homogeneous in plane 2—see Fig. 5c. However, the main message is again that the structure of the flow is complex and that the phase averaged data contain only one part of the structural information.

3.2 Quantification of structure fluctuations

It is particularly important to understand the cycle-to-cycle variation of an engine flow. Indeed, the quality of combustion in one given cycle is under the control of the mixing preparation in that given cycle. PIV is a very efficient tool to study cycle-to-cycle variations of the flow structure. Having performed the classical computation of RANS phase averages and before using more sophisticated statistical tools as POD, we therefore decided to carefully consider instantaneous velocity fields.

As an example, the horizontal mean velocity field for $\theta = 270$ CAD and $z = -15$ mm (Fig. 4c) is compared with three instantaneous velocity fields in Fig. 6a–c. A material circular curve γ centered on the mean zero velocity point is also shown in these figures. The radius (R) of γ was varied from $R = 5$ mm to $R = 20$ mm. The circulation (Γ) of the velocity field along the contour γ was then computed for all realizations of the velocity field. Γ is defined by:

$$\Gamma(R) = \int_{\gamma(R)} \mathbf{U}.\mathbf{dl} \tag{3}$$

In the following Γ (β) means the computation of Γ along the circle of radius $R = \beta$ mm. Γ is an integral quantity. Γ is equal to the integral of the vertical component of the vorticity over the disk of radius R. Statistics of Γ will be used in the following.
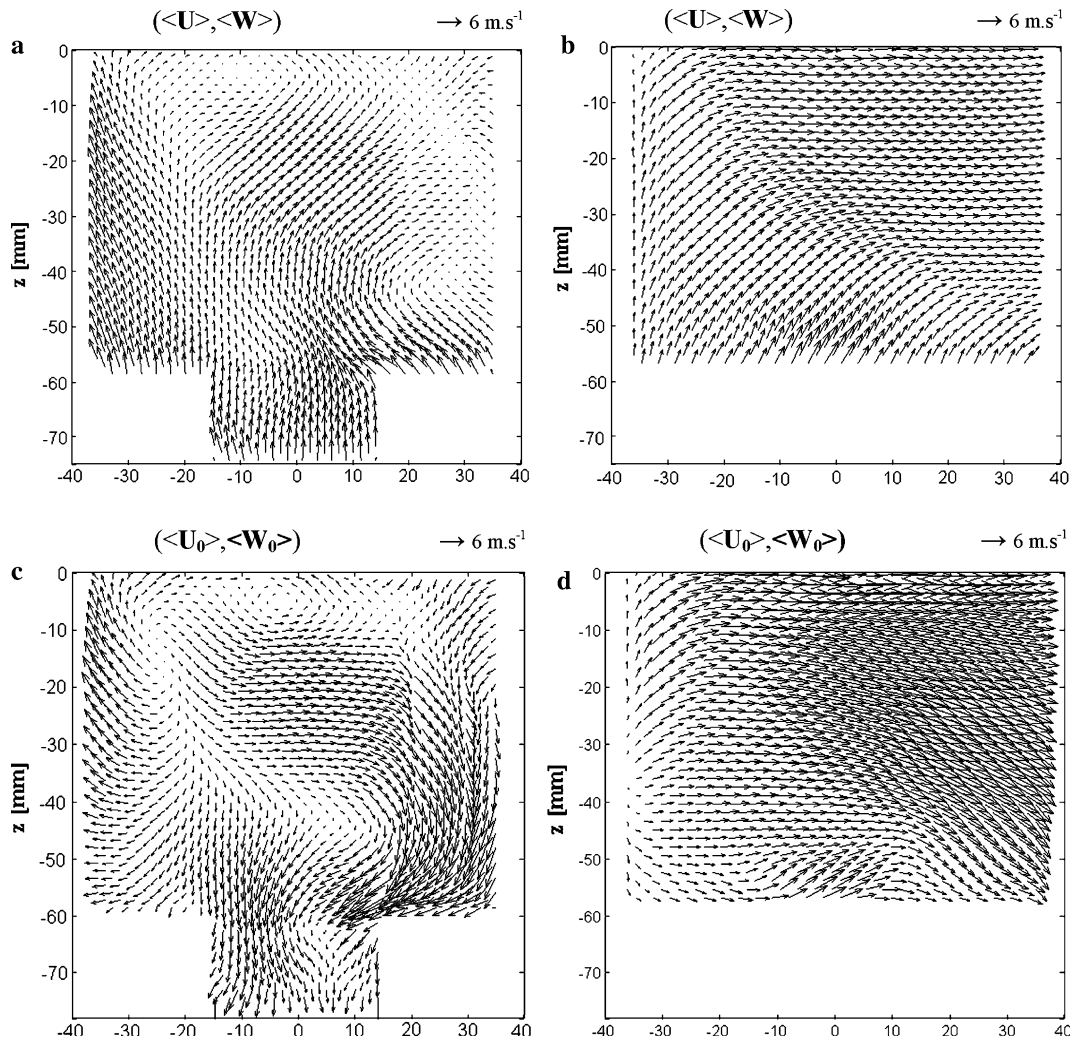

Fig. 5 Visualization of the phase-averaged velocity fields for vertical measurement planes, for $\theta = 270$ CAD: **a** plane 2, ($\langle U \rangle$, $\langle W \rangle$); **b** plane 5, ($\langle U \rangle$, $\langle W \rangle$); **c** plane 2, ($\langle U_0 \rangle$, $\langle W_0 \rangle$); **d** plane 5, ($\langle U_0 \rangle$, $\langle W_0 \rangle$)

Note that the Fig. 6a–c were not chosen randomly. In fact, they correspond to some instantaneous velocity fields having a value of $\Gamma(10)$ equal to $\Gamma(10) = \langle \Gamma(10) \rangle + A\sigma_{\Gamma(10)}$ from $A = +2$ (Fig. 6a) to $A = -2$ (Fig. 6c). $\langle \Gamma(10) \rangle$ is the phase averaged value of $\Gamma(10)$ and $\sigma_{\Gamma(10)}$ is its standard deviation: $\sigma_{\Gamma(R)} = \sqrt{\langle \Gamma'(R)^2 \rangle}$ with $\Gamma'(R) = \Gamma(R) - \langle \Gamma(R) \rangle$. Therefore, Fig. 6a corresponds to an instantaneous velocity field having one of the highest values of $\Gamma(10)$ among the statistical set. On the contrary, Fig. 6c corresponds to a flow realization having one of the lowest values of $\Gamma(10)$ in this set. Figure 6 therefore shows that the structure of the swirling flow is varying very significantly from one cycle to the other. A strong vortical motion is detected in the central region of Fig. 6a while a central low velocity kernel surrounded by a rotating annular region is detected in Fig. 6c.

Profiles of the U component of velocity along a y axis passing through the mean zero velocity point are drawn in Fig. 7a, b. The Fig. 7a corresponds to $\Gamma(10) = \langle \Gamma(10) \rangle + 2\sigma_{\Gamma(10)}$ (Fig. 6a) while the Fig. 7b is related to $\Gamma(10) = \langle \Gamma(10) \rangle - 2\sigma_{\Gamma(10)}$ (Fig. 6c). On both Fig. 7a, b, the mean velocity profile has been superimposed (dotted line). We see very clearly that the flow has switched from a "vortex type"—Fig. 7a—to an "annular type"—Fig. 7b—velocity field. The straight lines drawn in Fig. 7a, b are here to emphasize this change. Note that, for small values of R, it is possible to find negative values of the circulation Γ.

$$\Gamma(10) = \langle \Gamma(10) \rangle + 2\sigma_{\Gamma(10)}$$

$$\Gamma(10) = \langle \Gamma(10) \rangle$$

$$\Gamma(10) = \langle \Gamma(10) \rangle - 2\sigma_{\Gamma(10)}$$
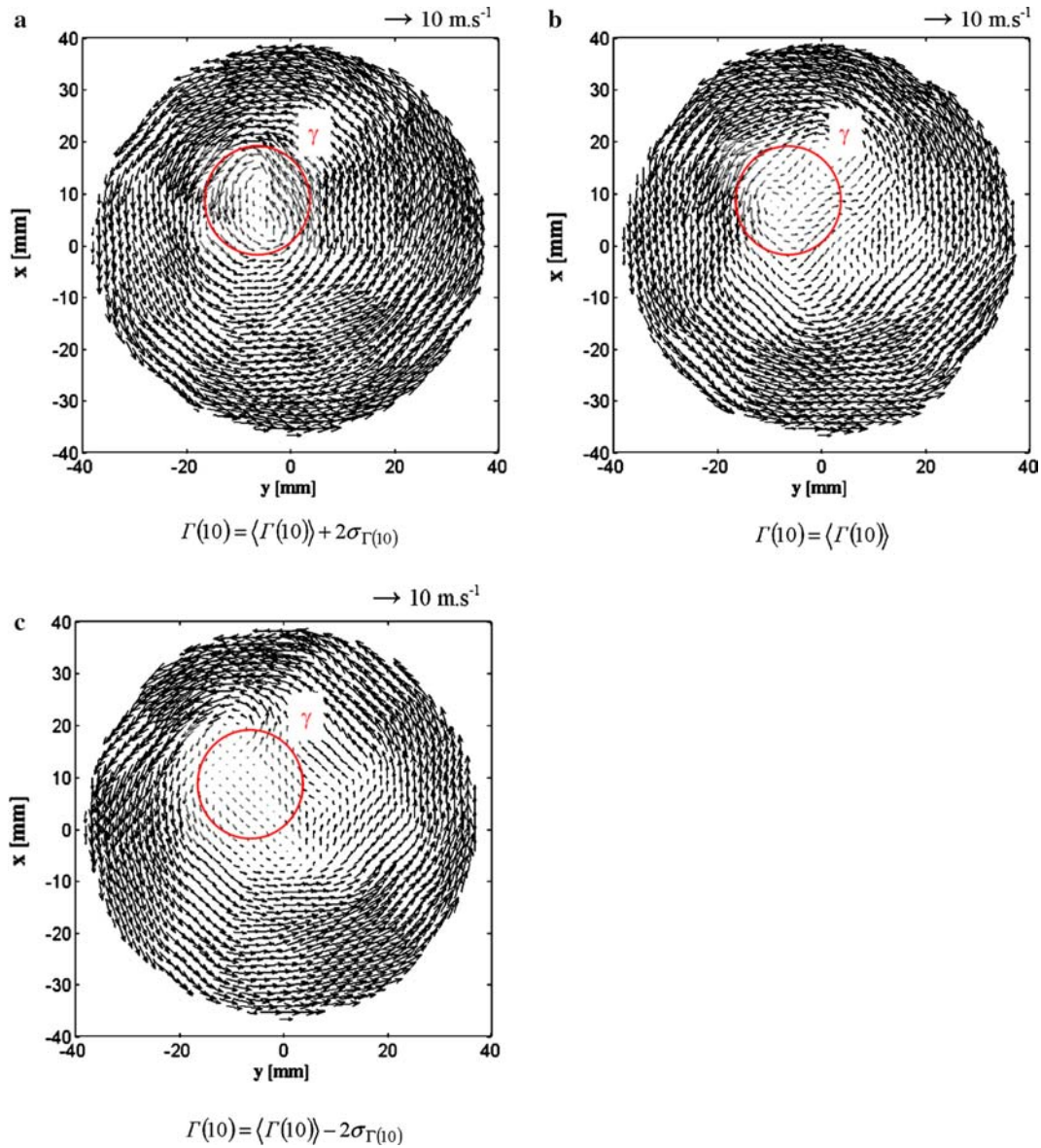
Fig. 6 Instantaneous horizontal velocity fields having a value of $\Gamma(10)$ equal to $\Gamma(10) = \langle \Gamma(10) \rangle + A\sigma_{\Gamma(10)}$ for $\theta = 270$ CAD, at $z = -15$ mm. **a** $A = +2$, **b** $A = 0$, **c** $A = -2$
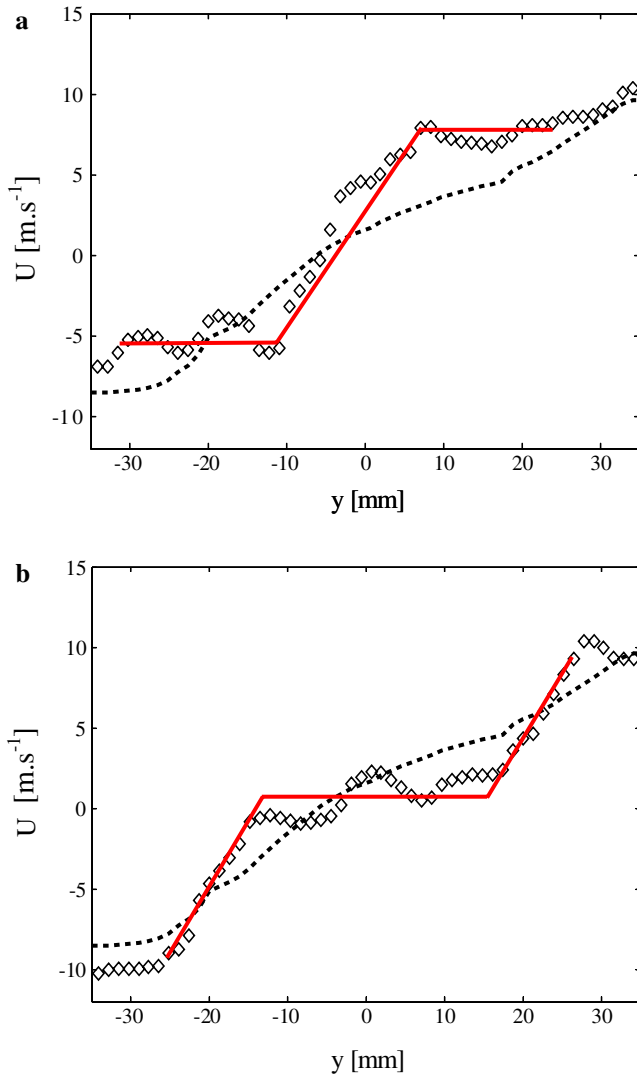
Fig. 7 Longitudinal velocity profile following y axis through the mean zero velocity point, for $\theta = 270$ CAD at $z = -15$ mm. **a** (*diamond*) $\Gamma(10) = \langle \Gamma(10) \rangle + 2\sigma_{\Gamma(10)}$, (...) mean velocity profile; **b** (*diamond*) $\Gamma(10) = \langle \Gamma(10) \rangle - 2\sigma_{\Gamma(10)}$, (...) mean velocity profile

These observations have very strong implications for the modeling of engine flows. First of all, phase averaged RANS models implicitly assume a large separation of scales between a mean flow and turbulent structures carried by this mean flow. They cannot deal with such structure variations. RANS/k-epsilon models will generally under-predict the measured turbulence intensity because they do not include large-scale cycle-to-cycle flow variations that are included in u' when it is evaluated as the rms fluctuation about the many-cycle phase or ensemble average. Therefore, URANS ("Unsteady RANS") or LES strategies should be proposed, even if their cost is much higher. Second, even if the instantaneous large scale structure of the flow was correctly predicted, it is very important to observe that velocity fields of "annular type" imply a very strong stabilizing effect on the turbulent field carried by the large scale flow (Bradshaw 1969). We know, for example, that eddy

viscosity models are unable to mimic such stabilizing effects. Their application would then result in an over-prediction of the turbulence intensity (Lumley 1999) and of its diffusive properties. Modeling issues must be considered very carefully in order to predict the good energy transfer between resolved and modeled scales of the flow.

The forcing of the swirling flow in the cylinder results from the interaction of the intake jets with the walls of the combustion chamber and from the mutual interaction of these jets. This should result in large scale unsteadiness during the intake phase not studied in detail during this work. The question is, however: Is turbulent diffusion intense enough to diffuse large scale non-uniformity of the momentum flux that could be induced during the intake stroke? An order of magnitude estimation can be obtained by following Lumley (1999). Note that stabilizing rotation effects are not taken into account in what follows. Let u' be the rms of the velocity and let's suppose that $u' \approx \bar{V}_p$ is a good estimation between $\theta = 180$ CAD and $\theta = 270$ CAD. The integral length scale is estimated as $l \approx b/6$ (Lumley 1999). The characteristic length affected by the turbulent diffusion of momentum is then given by $\delta \approx \sqrt{v_t t}$, where t is the time taken by the piston to move half way: $t \approx S/(2\bar{V}_p)$, where $S \approx b$ is the piston stroke. v_t is the turbulent diffusivity: $v_t \approx u' l$. We then obtain $\delta/b \approx 1/\sqrt{12} \approx 0.3$. The time available for the turbulent transport of momentum is therefore not large enough to enable a perfect smoothing of the swirling motion. Therefore, we feel that cycle-to-cycle differences, linked to structure instabilities, are expected.

Statistical information concerning the distribution of Γ are synthesized in Fig. 8a–d. The radius R of the circle γ is varied from 5 to 20 mm for all the measurement planes. Greater values of R can take account of points which are located outside the velocity fields and smaller values prevent from having a reasonable number of vectors for the calculation. The Fig. 8a, b shows that the mean value $\langle \Gamma \rangle$ is increasing with R. The shape of the curves indicate a square dependence on R and the log–log plot (Fig. 8b) confirm that the exponent is very close to $n = 2$. A solid body rotation would of course result in such an evolution while a point vortex or a Lamb-Oseen vortex of core radius much smaller than R would lead to a constant value of $\langle \Gamma \rangle$. We note here that the maximum values of "n" are found at $z = -7.5$ mm and $z = -2.5$ mm. The strength of the annular region is thus greater in the upper region close to the cylinder head. The radial evolutions of the standard deviation σ_Γ and of the fluctuation intensity $I_\Gamma = \sigma_\Gamma/\langle \Gamma \rangle$ are drawn in Fig. 8c, d. Except for the lowest measurement plane close to the bowl ($z = -45$ mm), the radius evolution of σ_Γ is first linear and then levels off for $R \geq 15$ mm. I_Γ is very strong for $R \leq 10$ mm. This means that zero—or even negative—values of Γ occur with a non-negligible probability. Such contours are therefore very good indicators of the structure fluctuations of the swirling flow. Γ being an integral quality, the decrease of I_Γ for larger radius is
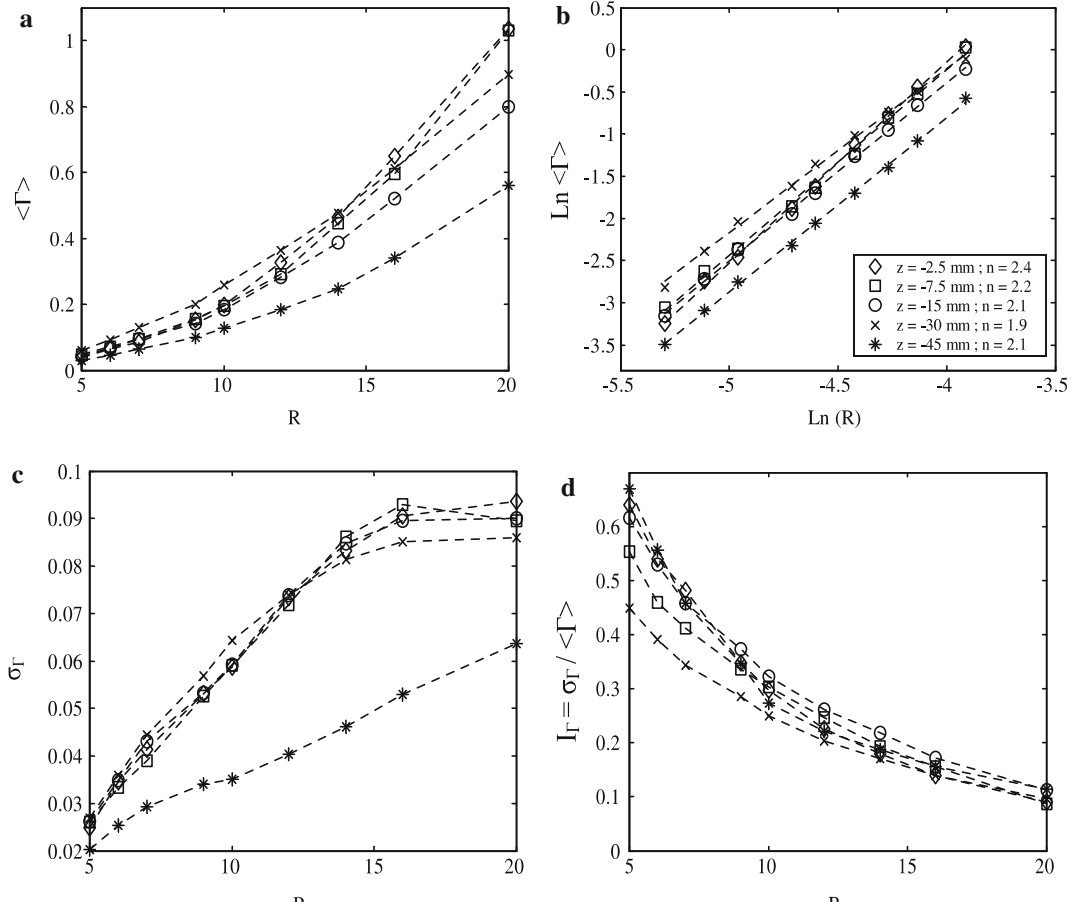
Fig. 8 Evolution of the circulation statistics as a function of the radius R of the curve γ, for the different horizontal measurement planes: **a** $\langle \Gamma \rangle$; **b** log–log plot of the mean circulation with a polynomial fitting of order unity—exponent n is defined according to $\mathrm{Ln}\langle \Gamma \rangle = n \ln(R) +$ Cste; **c** standard deviation σ_Γ; **d** $I_\Gamma = \sigma_\Gamma / \langle \Gamma \rangle$

expected. $I_\Gamma \approx 0.1$ at $R = 20$ mm is, however, a high value indicative of large cycle-to-cycle variations. Moreover, two normalized probability density functions are presented in Fig. 9 for $R = 10$ mm and $R = 20$ mm. We see that the normalized Gaussian distribution could be a good approximation for these pdf. Γ being a good global indicator of the structure fluctuations in this swirling flow, it is interesting to note that such Gaussian distribution was observed to fit the pdf for all the measurement planes. We therefore do not observe a bimodal distribution from "annular like" to "vortex like" structure but rather a continuous random distribution.
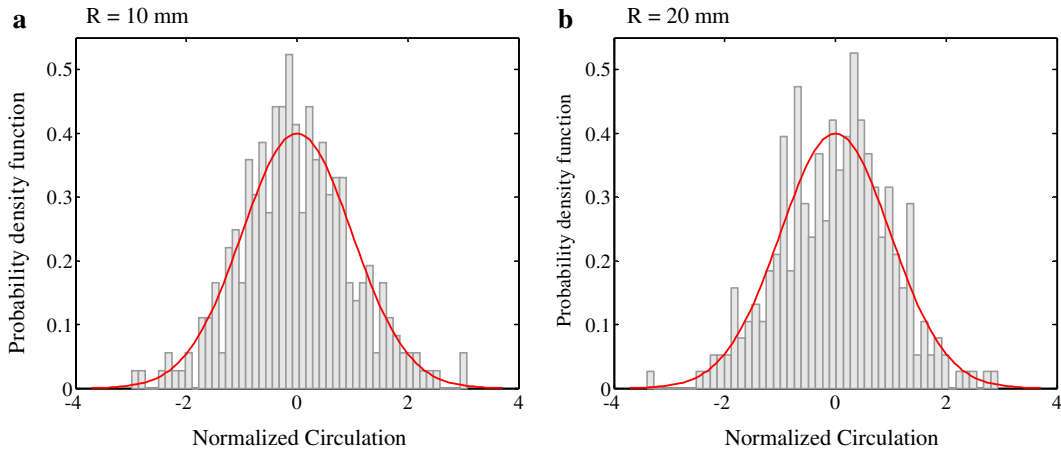

Fig. 9 Probability density function of normalized circulations for $\theta = 270$ CAD, at $z = -15$ mm, for two radius from the mean zero velocity point: **a** pdf for $R = 10$ mm, **b** pdf for $R = 20$ mm. A normalized Gaussian distribution (*line*) is superposed to the data
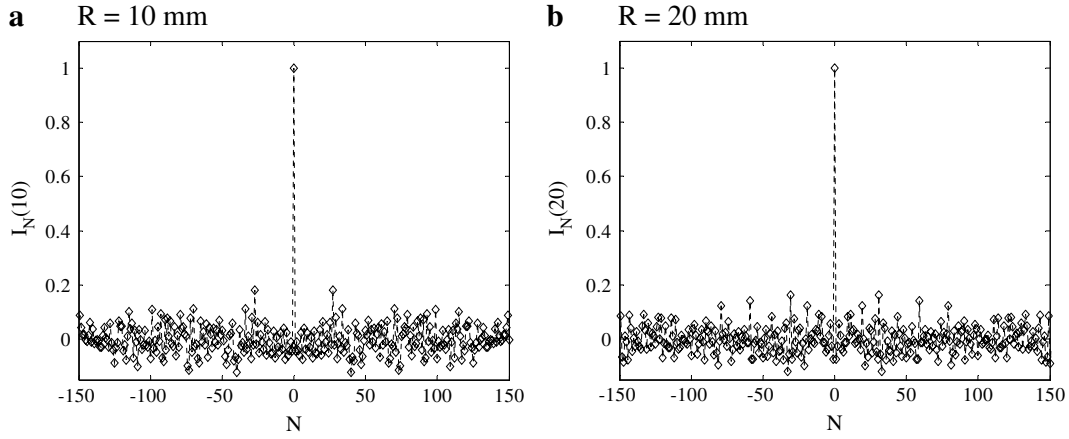
Fig. 10 Intercorrelations $I_N(R) = \langle \Gamma'_i(R). \Gamma'_{i+N}(R) \rangle / \sigma_i(R) \cdot \sigma_{i+N}(R)$ for $\theta = 270$ CAD at $z = -15$ mm. **a** $R = 10$ mm, **b** $R = 20$ mm

At a given engine cycle, one may wonder if the value of the circulation at large R is correlated or not to the value of Γ at moderate value of R. Namely, we ask if the structure of the core flow, characterized say by Γ (10), is indicative of the global amount of circulation in the given plane at that phase. The normalized correlation coefficient $I_{10,20} = \langle \Gamma'_i(10) \cdot \Gamma'_i(20) \rangle / \sigma_{\Gamma(10)} \cdot \sigma_{\Gamma(20)}$ was computed in the plane $z = -15$ mm. $\Gamma'_i(\beta) = \Gamma_i(\beta) - \langle \Gamma(\beta) \rangle$ is the fluctuating value of Γ in the cycle number i. We find $I_{10,20} \approx 0.45$. With only 300 independent velocity fields to estimate this correlation, the statistical uncertainty associated with this estimation is $\delta I_{10,20} \approx 0.046$ (Benedict and Gould 1996). We therefore show that, in a given cycle, we detect a correlation between values of Γ at moderate and large R in this engine.

Finally, it is important to remember that we have one realization of the PIV velocity field per consecutive engine cycle. Therefore, it is easy to check if Γ values are correlated or not. The Fig. 10a, b show the intercorrelation $I_N(R) = \langle \Gamma'_i(R).\Gamma'_{i+N}(R) \rangle / \sigma_{\Gamma_i(R)} \cdot \sigma_{\Gamma_{i+N}(R)}$. N therefore represents a systematic cycle shift. Owing to the number of velocity fields used to compute these evolutions, it is clear that instantaneous cycle-to-cycle values of Γ at either moderate or large radius and at different cycles are uncorrelated. Of course, this does not prove that $\Gamma_i(R)$ and $\Gamma_{i+N}(R)$ are strictly independent quantities. However, it seems to us a strong indication of the random nature of the structure variation of the swirling flow in the chamber of the Diesel engine.

3.3 Use of proper orthogonal decomposition

POD modes will be computed in the frame of the method of snapshots introduced by (Sirovich 1987). We appreciate that 300 fields per phase is a rather moderate number to perform a quantitative POD analysis. However, we maintain that the results, even qualitative, can be used for the study of this swirling flow.

The two-point correlation tensor at phase θ is approximated by:

$R(\mathbf{x}, \mathbf{x}') = \langle \mathbf{U_n}(\mathbf{x})\mathbf{U_n}(\mathbf{x}') \rangle = \frac{1}{M} \sum_{n=1}^{M} \mathbf{U_n}(\mathbf{x})\mathbf{U_n}(\mathbf{x}')$.
$\mathbf{U_n}(x,y)$ is the individual event, here the instantaneous velocity field. M is the number of independent events in the PIV datasets. Vector multiplication denotes a Dyadic product. The fields are all real, and the matrices symmetric, so that the eigenvectors and eigenvalues are real.

M eigenfunctions $\Phi^{(k)}(x,y)$ and positive eigenvalues $\lambda^{(k)}$ ($k = 1,..., M$) are obtained with: $\Phi^{(k)}(x,y) = \sum_{n=1}^{M} c_n^{(k)} \mathbf{U_n}(x,y)$. The constants $c_n^{(k)}$ are eigenvectors of the matrix $C = [(\mathbf{U_n}, \mathbf{U_p})/M]$ and $\lambda^{(k)}$ corresponds to the associated eigenvalues. Here, $(\mathbf{U_n}, \mathbf{U_p})$ denotes the inner product $(\mathbf{U_n}, \mathbf{U_p}) = \int_S \mathbf{U_n}(x,y) \mathbf{U_p}(x,y) \, dxdy$.

Having solved the POD problem, each instantaneous flow field component can be projected onto the POD basis to obtain:

$$\mathbf{U_n}(x,y) = \sum_{k=1}^{M} a_n^{(k)} \Phi^{(k)}(x,y) \qquad (4)$$

$\Phi^{(k)}(x,y)[k = 1, M]$ are the POD modes associated to the eigenvalues $\lambda^{(k)}$. The eigenvalues are real and $\lambda^{(k)} > \lambda^{(k+1)}$. The modes form an orthonormal basis. Thus, we have: $(\Phi^{(k)}, \Phi^{(l)}) = \delta_{kl}$. $a_n^{(k)} = (\mathbf{U_n^{(k)}}, \Phi^{(k)})$ are the random reconstruction coefficients. These coefficients are uncorrelated with $\langle a_n^{(k)} \cdot a_n^{(l)} \rangle = \lambda^{(k)} \delta_{kl}$. This general statistical theory is well adapted to problems in turbulence study as it provides a diagonal decomposition of the correlation tensor and an optimal decomposition of the kinetic energy [E] integrated over the flow domain analyzed with POD: $E = \langle (\mathbf{U_n}, \mathbf{U_n}) \rangle = \sum_{k=1}^{M} \lambda^{(k)}$.

This statistical decomposition is of course richer than the Reynolds decomposition leading to $E = \langle (\mathbf{U_n}, \mathbf{U_n}) \rangle = (\langle \mathbf{U_n} \rangle, \langle \mathbf{U_n} \rangle) + \langle (\mathbf{u_n}, \mathbf{u_n}) \rangle$. We will apply the decomposition to the total velocity field and not to the fluctuating velocity field. Indeed, if structure variation is a property of the flow, it seems important to us not to subtract a priori a phase averaged field.

From the POD decomposition, some authors (see e.g. Bonnet et al. 2002 and references therein) propose to

126

define a truncated velocity field $\mathbf{U_n^{\leq m}}(x,y)$ defined as a projection onto the "$m \leq M$" first POD modes: $\mathbf{U_n^{\leq m}}(x,y) = \sum_{k=1}^{m} a_n^{(k)} \Phi^{(k)}(x,y)$. The main difficulty with this approach consists in the choice of a truncation order. We will discuss this problem by using the integral indicators in the following.

The four first POD modes in the plane $z = -15$ mm are drawn in Fig. 11a–d. The cumulative sum of POD eigenvalues in this decomposition is presented in Fig. 12. The Fig. 12 shows that the first mode contains the major part of the total kinetic energy E (between 85 and 92% according to the plane). However, the convergence of the POD spectrum is quite slow. Moreover, it is not possible to detect any "cut-

off" mode number from the continuous evolution in Fig. 12. In Fig. 11, we see that modes 2, 3 and 4 have a complex structure, much more complex than the typical second and third modes obtained when analyzing the random displacement of a model axisymmetric vortex—see for instance (Graftieaux et al. 2001). In our situation, it is interesting to note that low order modes possess significant energy content in the core region. They should therefore be indicative of strong fluctuations of the flow structure.

An instructive model problem can be considered if we truncate the POD decomposition using only the first POD mode. With $\mathbf{U_n^{\leq 1}}(x,y) = a_n^{(1)} \Phi^{(1)}(x,y)$, the structure of the flow is fixed and is close to the phase averaged
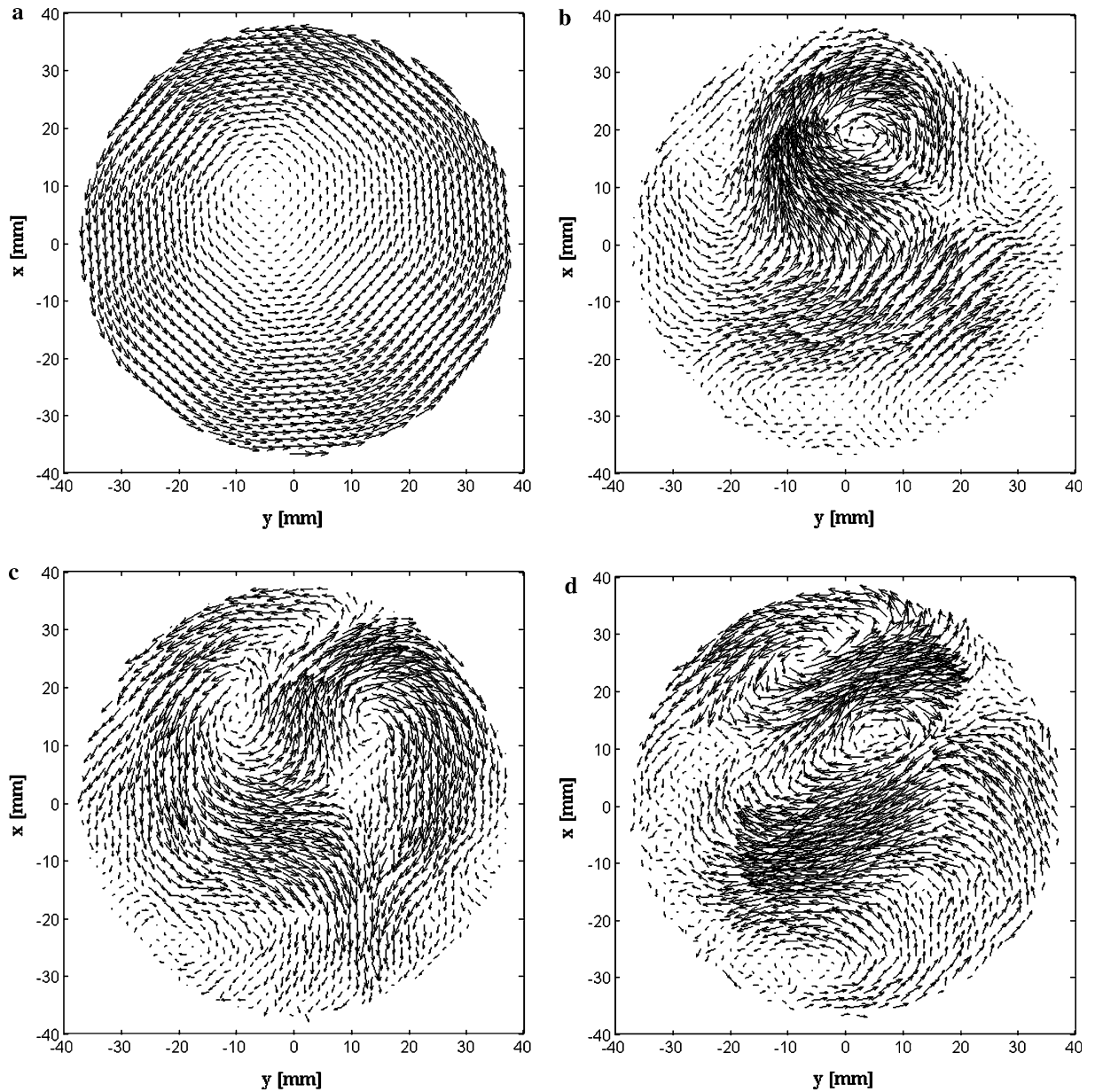

Fig. 11 Visualization of POD modes of the flow, for $\theta = 270$ CAD at $z = -15$ mm: **a** first mode; **b** second mode; **c** third mode; **d** fourth mode
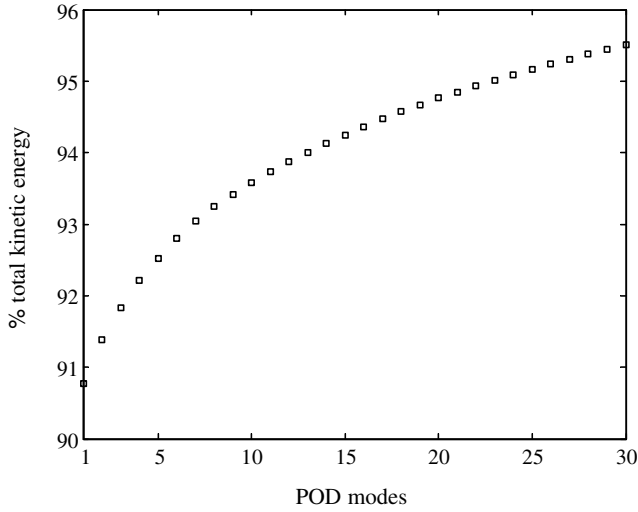
Fig. 12 Cumulative sum of POD eigenvalues, representing the percentage of the total kinetic energy of the flow, for $\theta = 270$ CAD at $z = -15$ mm. Only 30 first modes are presented here

velocity field (compare Figs. 11a and 4c). The random nature of $a_n^{(1)}$ only influences the modulus of the velocity everywhere in the flow. The Table 3 presents values of the mean and standard deviation of $a_n^{(1)}$ for each plane. We note that deviations from the mean are quite strong with $I_1 = \sigma_1 / \langle a_n^{(1)} \rangle \approx 5\%$.

If this truncated flow field is used to compute the circulation $\Gamma_n^{\leq 1}(R)$, we find $\Gamma_n^{\leq 1}(R) = a_n^{(1)} . \int_\gamma \Phi^{(1)} . \mathbf{dl}$. The integral of $\Phi^{(1)}$ being a deterministic quantity, it is then obvious to show that $I_1 \approx 5\%$ is equal to the fluctuation intensity of $\Gamma_n^{\leq 1}(R)$ whatever the value of R. Considering again Fig. 8d, we therefore see that I_1 is much smaller than I_Γ, particularly for moderate values of the radius R of the circle $\gamma(R)$. Higher order modes have therefore to be taken into account to describe the structure variation of the swirling flow.

We come back to the study of the full velocity field. The circulation data can be decomposed using the POD decomposition (Eq. 4):

$$\Gamma_n(R) = \int_\gamma \mathbf{U_n}.\mathbf{dl} = \sum_{k=1}^{M} a_n^{(k)} \int_\gamma \Phi^{(k)}.\mathbf{dl} = \sum_{k=1}^{M} b_n^{(k)} \Gamma^{(k)}(R),$$
(5)

where $b_n^{(k)} = a_n^{(k)} / \sqrt{\lambda^{(k)}}$ and $\Gamma^{(k)}(R) = \sqrt{\lambda^{(k)}} \int_{\gamma(R)} \Phi^{(k)}.\mathbf{dl}$.

Table 3 Characteristics of the first POD mode according to the measurement plane

Plane location	$\lambda_1 (10^5)$	% E	$\langle a_n^{(1)} \rangle$	σ_1	I_1 (%)
$z = -2.5$	3.7	92.5	609.3	33.5	5.5
$z = -7.5$	4.0	93.5	635.5	26.4	4.2
$z = -15$	2.3	90.7	483.1	24.3	5.0
$z = -30$	2.7	84.7	520.5	25.4	4.9
$z = -45$	1.2	86.74	344.6	20.3	5.9

$b_n^{(k)}$ are the normalized random coefficients with $\langle b_n^{(k)} . b_n^{(p)} \rangle = \delta_{kp}$. Statistical moments of $\Gamma_n(R)$ can easily be computed with $\langle \Gamma_n \rangle = \sum_{k=1}^{M} \langle b_n^{(k)} \rangle \Gamma^{(k)}$ and $\langle \Gamma_n . \Gamma_n \rangle = \sum_{k=1}^{M} [\Gamma^{(k)}]^2$. The fluctuation intensity $I_\Gamma = \sigma_\Gamma / \langle \Gamma \rangle$ then simply can be written:

$$I_\Gamma^2 = \frac{\langle \Gamma_n . \Gamma_n \rangle - \langle \Gamma_n \rangle^2}{\langle \Gamma_n \rangle^2} = \sum_{k=1}^{M} \frac{\Gamma^{(k)^2}}{\langle \Gamma_n \rangle^2} - 1$$
(6)

It is therefore possible to determine the modes contributing to the fluctuation of the circulation. The truncated values $\langle \Gamma_n \rangle^{\leq m}$ and $I_\Gamma^{\leq m}$ are defined by summing only over $m \leq M$ POD modes. The convergences of these truncated values as a function of the radius R of the circle γ are studied in Fig. 13.

The mean value $\langle \Gamma_n \rangle^{\leq m}$ converges rapidly. Figure 13a shows that for $m = 1$, the mean circulation can be recovered at all values of R. The truncated value $I_\Gamma^{\leq m}$ has a different behavior, since the convergence is definitely not so fast. In fact, Fig. 13b reveals that two regions of the flow field have to be considered. First, for $R \geq 12$ mm, convergence can be assumed for $m = 5$. That means that the fluctuation of circulation for large R might be correctly represented by the first 5 modes. Second, for $R < 11$ mm, convergence of $I_\Gamma^{\leq m}$ is very slow and a large number of modes are necessary to represent the fluctuation of the circulation in the kernel (more than 10 modes is a necessity).

Finally, one may wonder if the random coefficients $b_n^{(k)}$ can be used to detect easily a particular structure of the flow field in this engine. The absolute value of the correlation coefficient between these normalized values can be estimated, since it can be written:

$$P^{(k)}(R) = \left| \left\langle (\Gamma_n'/\sigma_\Gamma).b_n^{(k)} \right\rangle \right| = \left| \frac{1}{\sigma_\Gamma} \left[\Gamma^{(k)} - \left\langle b_n^{(k)} \right\rangle \langle \Gamma_n \rangle \right] \right|.$$
(7)

The evolution of $P^{(k)}(R)$ as a function of the mode number k and for $R = 10$ mm is drawn in Fig. 14. We see that $P^{(k)}(R) \approx 0.5$ for $k = 3$ and $k = 4$. The associated clouds of points, plotted in Fig. 15a, b, indeed show that these normalized random coefficients might be used to detect a particular structure of the flow field in the engine—for example, low values of Γ should be associated with respectively large negative values of $b_n^{(3)}$ and large positive values of $b_n^{(4)}$. The evolution of $P^{(k)}(R)$ with the radius R is plotted in Fig. 16 for $k = 1$ to 8. It shows that the contributions of the third and fourth modes always dominate.

4 Analysis of the flow at the end of the compression stroke

Around $\theta = 330$ CAD, the flow transfer from the cylinder bulk to the bowl is known to produce shear layers, which are favorable to generate turbulence. Then, this transfer induces toroïdal or tumble flows in the bowl
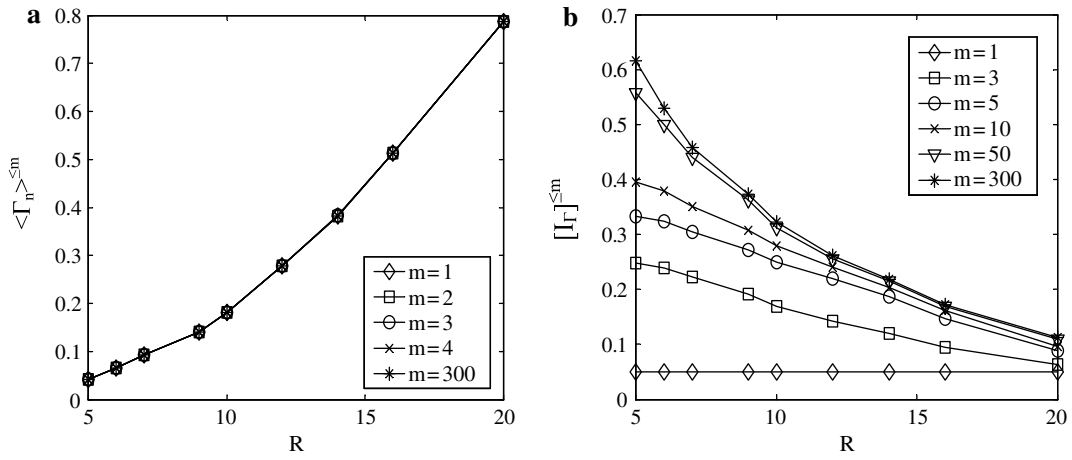
Fig. 13 Truncated values $\langle \Gamma_n \rangle^{\leq m}$ and $[I_\Gamma]^{\leq m}$ as a function of the radius R (mm) of the circle $\gamma(R)$. **a** $\langle \Gamma_n \rangle^{\leq m}$; **b** $[I_\Gamma]^{\leq m}$
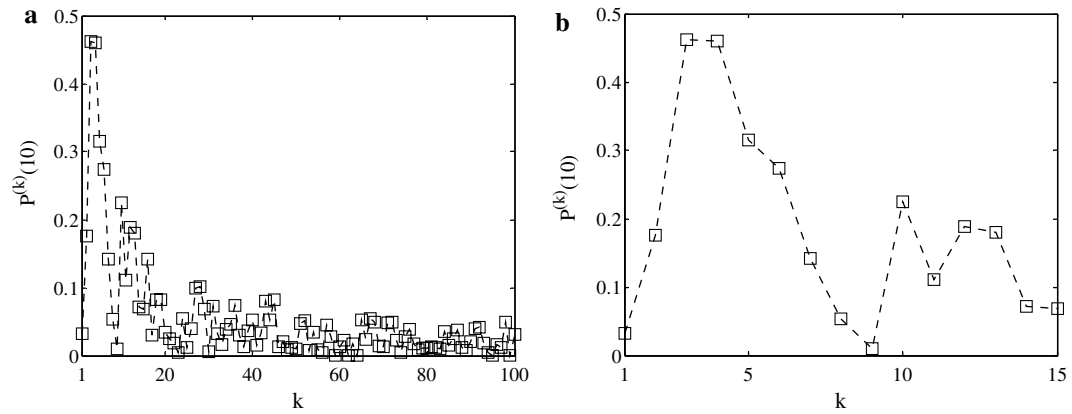

Fig. 14 Absolute value of the correlation coefficient between Γ_n'/σ_Γ and $b_n^{(k)}$ for $R = 10$ mm. **a** 100 first modes; **b** 15 first modes
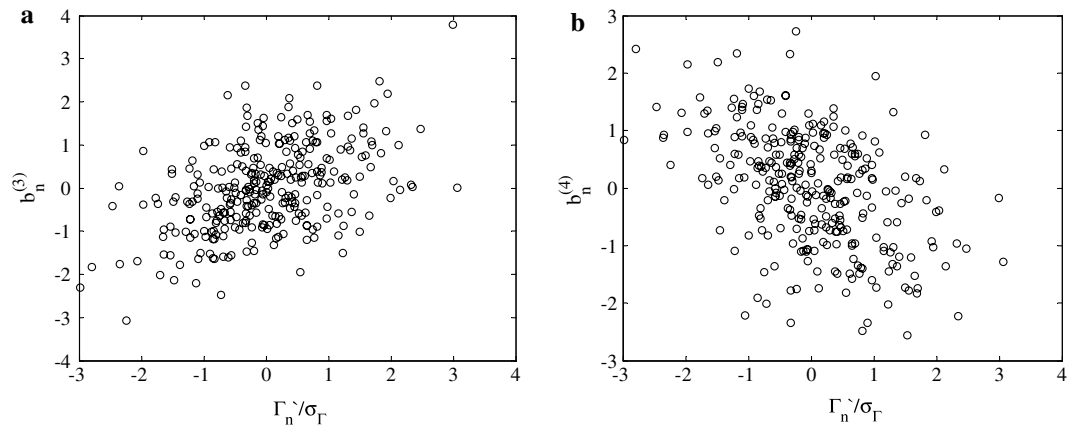

Fig. 15 Clouds of points $(\Gamma_n'/\sigma_\Gamma, b_n^{(k)})$ for $R = 10$ mm. **a** $k = 3$, **b** $k = 4$

interacting with the swirling air motion. This interaction between squish phenomenon and the swirling flow is currently under investigation. We only focus the discussion here on the top dead center. In this state, the flow is mainly confined in the cylindrical bowl, for the separating distance between the roof and the piston crown is about 0.7 mm. Analyses have been undertaken in three planes, as shown in Fig. 2.
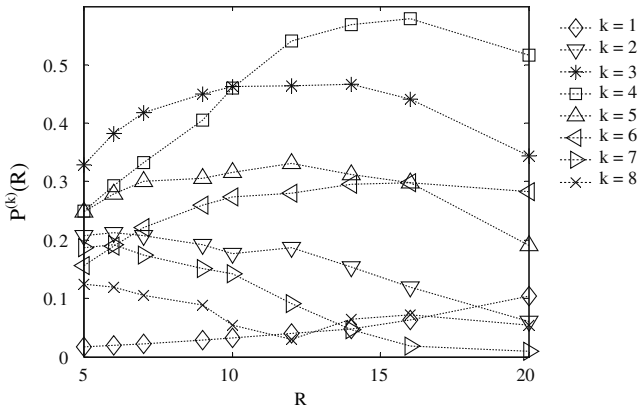
Fig. 16 Evolution of $P^{(k)}$ (R) with R, for $k = 1$ to $k = 8$

The question examined here is whether the large scale structure fluctuations detected at the mid-compression phase remain at TDC after the strong squish motion. Obtaining the PIV flow fields was not an easy task because of the confinement and the severe thermodynamical conditions.

4.1 Mean flow analysis

First of all, we look at the global patterns of the flow within the bowl by analyzing the phase-averaged velocity fields (see Fig. 17a–c). An organized swirling structure is observed for the three measurement planes. However, one can distinctly see—and particularly in Fig. 17a—that a mean out of plane 3D motion is ex-
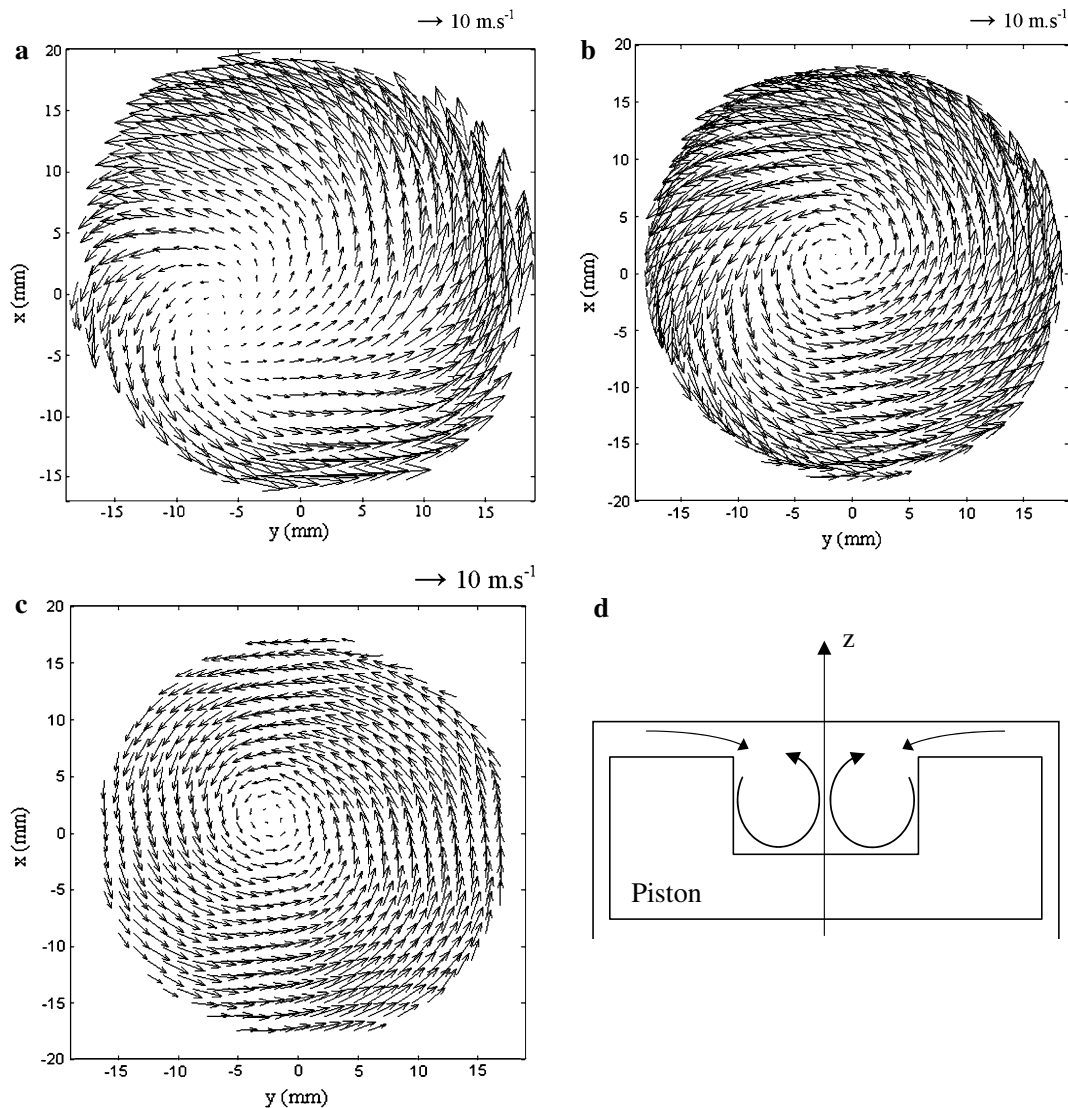

Fig. 17 Phase-averaged velocity fields at TDC, for the three measurement planes and schematic view of the toroidal motion at TDC. **a** $z = -2.5$ mm; **b** $z = -7.5$ mm; **c** $z = -2.5$ mm; **d** inversion of the toroidal motion in the presence of a high swirling component

pected. To precisely prove that this observation is linked with a three-dimensional state of the flow, the vertical velocity gradient has been computed. Continuity equation gives:

$$\frac{\partial \langle U \rangle}{\partial x} + \frac{\partial \langle V \rangle}{\partial y} + \frac{\partial \langle W \rangle}{\partial z} = -\frac{1}{\rho}\frac{\partial \rho}{\partial t}, \qquad (8)$$

where ρ is the density of the air submitted to compression. At TDC, the instantaneous piston velocity is zero and $\partial \rho / \partial t \approx 0$. Thus:

$$\frac{\partial \langle W \rangle}{\partial z} = -\left[\frac{\partial \langle U \rangle}{\partial x} + \frac{\partial \langle V \rangle}{\partial y}\right] \qquad (9)$$

Consequently, the out-of-plane velocity gradient is computed using the planar divergence of the two-dimensional velocity field resolved by PIV. The contours of $\partial \langle W \rangle / \partial z$ are not presented here for brevity but the spatial average value of $\overline{\partial \langle W \rangle / \partial z}$ in the central region of the bowl (Disk of radius 5 mm) is listed in Table 4. The magnitude of $\overline{\partial \langle W \rangle / \partial z}$ is higher near the roof of the cylinder and this indicates a strong 3D motion. Moreover, the signs are the signature of an upward mean motion of the flow in the central part of the bowl (Fig. 17d). Squish induces toroidal motion in the bowl, which can be inversed due to the interaction of the squish motion with a high swirl (Arcoumanis et al. 1983; Fansler and French 1987, 1988). The motion revealed by the signs of $\partial \langle W \rangle / \partial z$ is typical of this phenomenon. Figure 18a, b corresponds to the vertical measurement in the bowl at TDC; it shows the mean velocity field in planes 1 and 2, confiming the sketch 17d and revealing the upward mean motion in the central zone of the bowl.

4.2 Large scale fluctuations and circulation statistics

The horizontal mean velocity field at $z = -7.5$ mm (Fig. 17b) can again be compared with instantaneous realizations of the flow in that plane displayed in Fig. 19a, b. The Fig. 19a corresponds to an instantaneous velocity field having a value $\Gamma (5) = \langle \Gamma (5) \rangle + 2\sigma_{\Gamma (5)}$, on the other hand, $\Gamma (5) = \langle \Gamma (5) \rangle - 2\sigma_{\Gamma (5)}$ in Fig. 19b. While Fig. 19a exhibits a strong rotating motion, a very low velocity kernel is still detected in Fig. 19b. $\Gamma (5)$ is the circulation computed along the circle of radius $R = 5$ mm centered on the mean zero velocity point. Note that the ratio between the cylinder radius and the bowl is 2.1. $R = 5$ mm at TDC would therefore correspond geometrically to $R \approx 10$ mm at 270 CAD. This important observation means that we still detect structure fluctuations of the swirling flow at TDC after the squish phase. The instantaneous velocity profiles of Fig. 20 confirm this cycle-to-cycle variation in the flow structure. Although the shear layers induced by squish produce turbulence, this turbulence occurs very near TDC. The squish motion may be too late and associated to a too weak turbulent diffusivity ($v_t \approx u'.l$)

Table 4 Average value of $\overline{\partial \langle W \rangle / \partial z}$ in the central θ region of the bowl (Disk of radius 5 mm)

	$z = -15$ mm	$z = -7.5$ mm	$z = -2,5$ mm
$\overline{\partial \langle W \rangle / \partial z}$	> 0 (410.58)	< 0 (−68.05)	< 0 (−298.77)

(Lumley 1999). Therefore, it cannot smooth out the structure variations identified at the mid-compression phase.

In order to compare with mid-compression data, $\langle \Gamma \rangle$ and I_Γ at both $\theta = 270$ CAD and at TDC are plotted in Fig. 21a, b as a function of a normalized radius R^*: $R^* = 2R/b$ is used at $\theta = 270$ CAD while $R^* = 2R\, d_b$ is used at $\theta = 360$ CAD (d_b is the diameter of the bowl). If Kelvin theorem was valid for the mean velocity field in the present case, we should observe a conservation of the circulation along mean material circular lines. As the transfer in the bowl is quasi complete at $\theta = 360$ CAD, we should then observe $\langle \Gamma (R^*) \rangle_{\theta = 360°} = \langle \Gamma (R^*) \rangle_{\theta = 270°}$. The Fig. 21a shows that this is not the case. A crude estimation indicates that the circulation in the bowl, for the same non-dimensional radius R^*, is half the circulation in the cylinder. Losses due to turbulence and transfer of mean vorticity from vertical to azimuthal direction during the generation of the mean 3D motion in the bowl should be responsible for such angular momentum decrease.
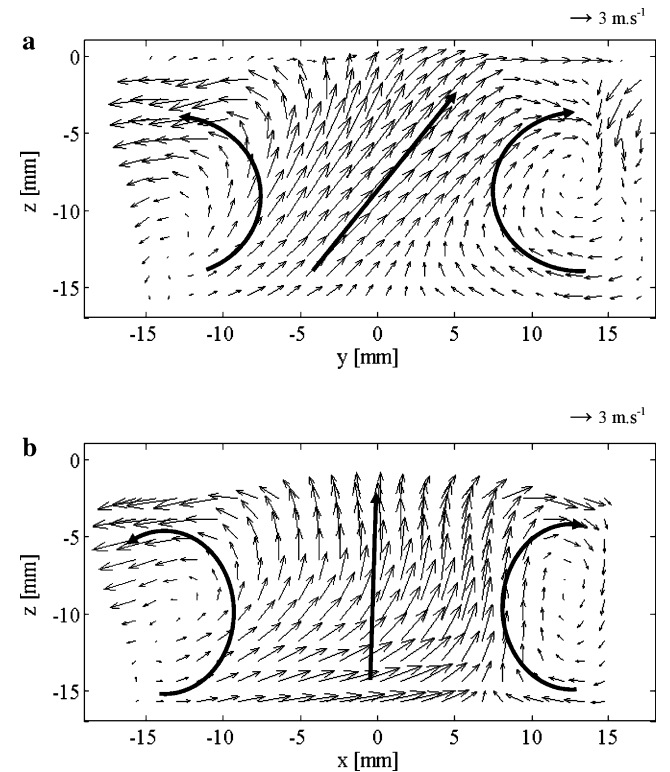

$\rightarrow$ 3 m.s^{-1}

$\rightarrow$ 3 m.s^{-1}

Fig. 18 Vertical phase-averaged velocity fields at TDC, for two measurement planes. **a** plane 1; **b** plane 2
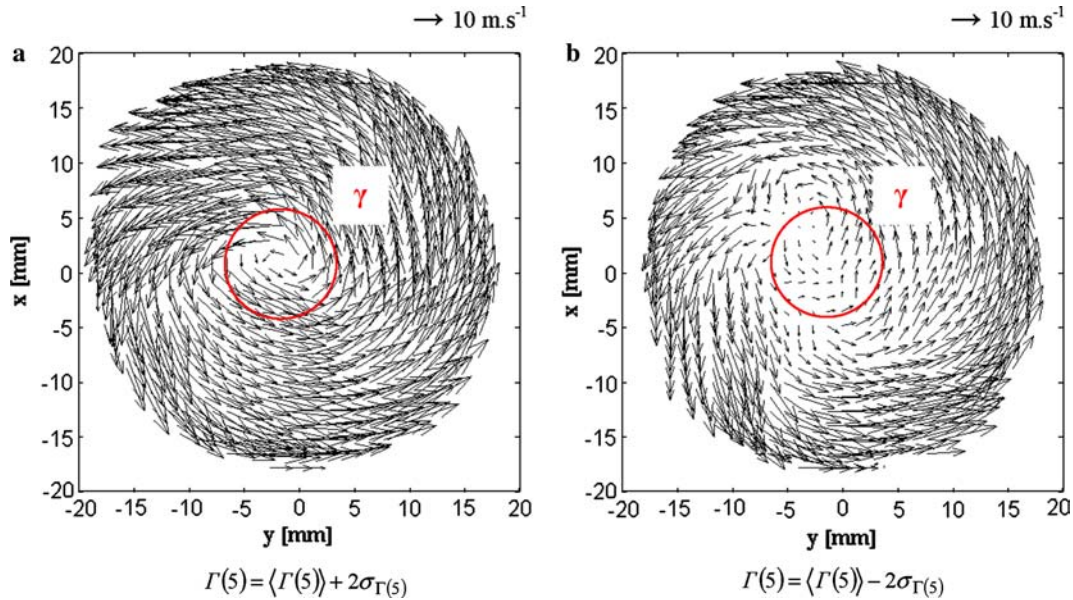
Fig. 19 Instantaneous horizontal velocity fields having a value of Γ (5) equal to Γ (5) $= \langle \Gamma$ (5)$\rangle + A\sigma_{\Gamma\,(5)}$ for $\theta = 360$ CAD, at $z = -7.5$ mm. **a** $A = +2$; **b** $A = -2$

The Fig. 21b is believed to be interesting. It shows clearly that the fluctuation intensity of circulation plotted as a function of R^* follow a similar evolution at $\theta = 270$ CAD and $\theta = 360$ CAD. In fact, TDC data in the plane $z = -7.5$ mm corresponding to the central plane of the bowl closely follow the results discussed in part 3. I_Γ is high for $R^* < 0.2$ and I_Γ decreases to about $I_\Gamma \approx 0.05$ for $R^* > 0.6$. We also see in Fig. 21b that I_Γ is significantly larger at TDC in near wall planes corresponding either to the roof of the cylinder or the bottom of the bowl. Strong confinement and flow interaction with walls are expected to produce such structure fluctuation near walls. More analysis is still required to understand this point. A POD analysis was also performed at TDC but is not repeated here for brevity. The major conclusion of this last section is indeed that the structure variations of the swirling flow survive up to TDC in Diesel engines.

5 Concluding remarks

PIV data obtained in a transparent motored Diesel engine were discussed in this paper. The research engine was developed by RENAULT s.a.s. in order to improve the understanding of the flow structure and the cyclic variations of the swirling flow. The knowledge of the bulk motion and of the turbulence evolution in the cylinder is indeed of great importance for the improvements of these engines.

These data were obtained in severe thermodynamical conditions in the cylinder during the cycle and in the bowl at TDC. Moreover, they were obtained at consecutive cycles. We first focused our analysis on the middle of the compression phase at 270 CAD. Phase averaged mean velocity fields in horizontal and vertical planes were analyzed. Even if a mean swirl is measured, we have shown that the structure of the mean flow is complex and difficult to interpret because the phase averaged data contain only one part of the structural information. Instantaneous velocity fields at 270 CAD were analyzed and classified by using an integral indicator based on the circulation Γ (R) of the velocity field along a circle of radius R centered on the mean zero velocity point. An important result is that the structure of the swirling flow is varying very significantly from "vortex type" to "annular type" from one cycle to the other. A physical analysis shows that such structure variations should result from the forcing of the swirling flow during the intake phase and that the time available for the turbulent transport of momentum is not large enough to enable a perfect smoothing of the swirling motion. It is therefore important to obtain statistics of these structure variations.

Statistics of Γ (R) were analyzed. For example, the fluctuation intensity I_Γ of Γ is very strong for $2R/b \leq 1/4$. Moreover, with $I_\Gamma \approx 10\%$ for $2R/b \approx 1/2$, we show that large cycle-to-cycle variations occur in this research engine. Intercorrelations of in-cycle and inter-cycle data were also computed. In particular, we do not find any cycle-to-cycle correlation.

Sophisticated statistical decompositions, like proper orthogonal decomposition, are often applied to engine flows. The goal is to extract from the velocity field some coherent features which may provide a description of the large scale motion variability in engine flows. The POD decomposition was applied to the statistical set of velocity fields. The convergence of the POD spectrum is

quite slow and it seems impossible to detect any "cut-off" mode number from this spectrum [that is to say from a kinetic energy criterion]. The circulation data were then decomposed using the POD approach and we have shown that the first and second order moments of $\Gamma(R)$ are reasonably converged if more than 10 modes is kept. Normalized random coefficients were also shown to provide good indicators of the structure of the instantaneous swirling flow.

Finally, we presented an analysis of the in-bowl flow at the very end of the compression phase. The main result is that we still detect qualitatively and quantitatively strong structure fluctuations of the swirling flow at TDC after the squish phase. For example, the normalized circulation fluctuation intensities follow a similar evolution at 270 CAD and TDC. The squish motion may be too late and associated to a too weak turbulent

diffusivity. As a consequence, the structure variations of the swirling flow therefore survive up to TDC in this research Diesel engine.

The results presented here have important consequences for the modeling of engine flows. In particular, they once more show that it is not possible to assume any separation of scales between a mean flow and turbulent structures carried by this mean flow. They also open a lot of questions. We believe that it is very important to improve our understanding of the generation of this large scale variability. Both numerical and experimental approaches should be combined to achieve such understanding. Finally, it might be possible to reduce the statistical complexity by finding low-order descriptions of the large scale flow during a cycle. In this, there should be close links with methods developed for flow control applications in external and internal aerodynamics.
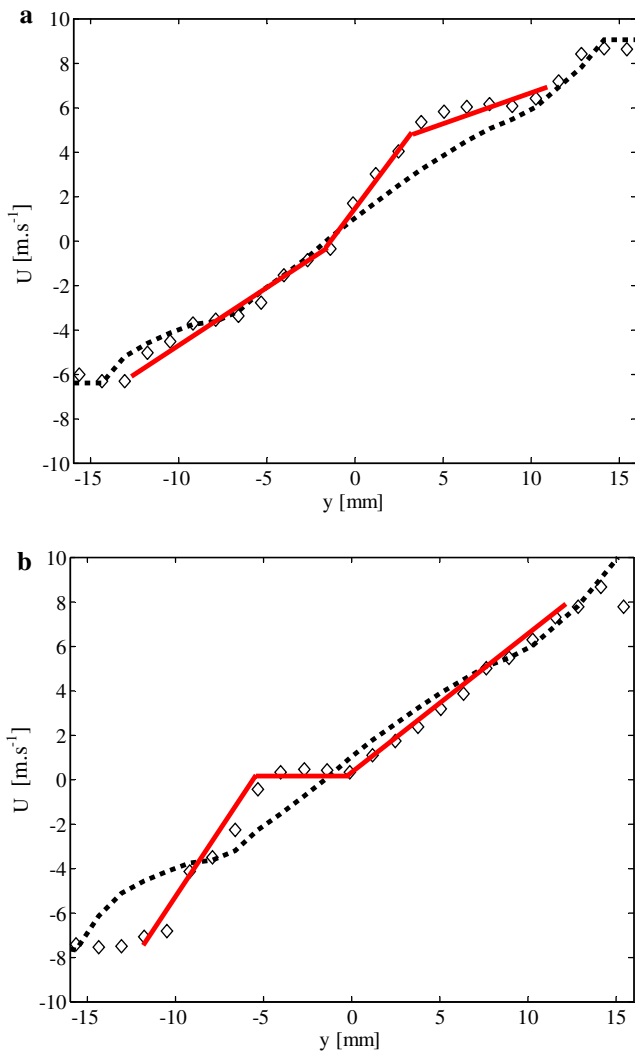

Fig. 20 Longitudinal velocity profile following y axis through the mean zero velocity point, for $\theta = 360$ CAD at $z = -7.5$ mm. **a** (*diamond*) $\Gamma(5) = \langle \Gamma(5) \rangle + 2\,\sigma_{\Gamma(5)}$ (...) mean velocity profile; **b** (*diamond*) $\Gamma(5) = \langle \Gamma(5) \rangle - 2\sigma_{\Gamma(5)}$ (...) mean velocity profile
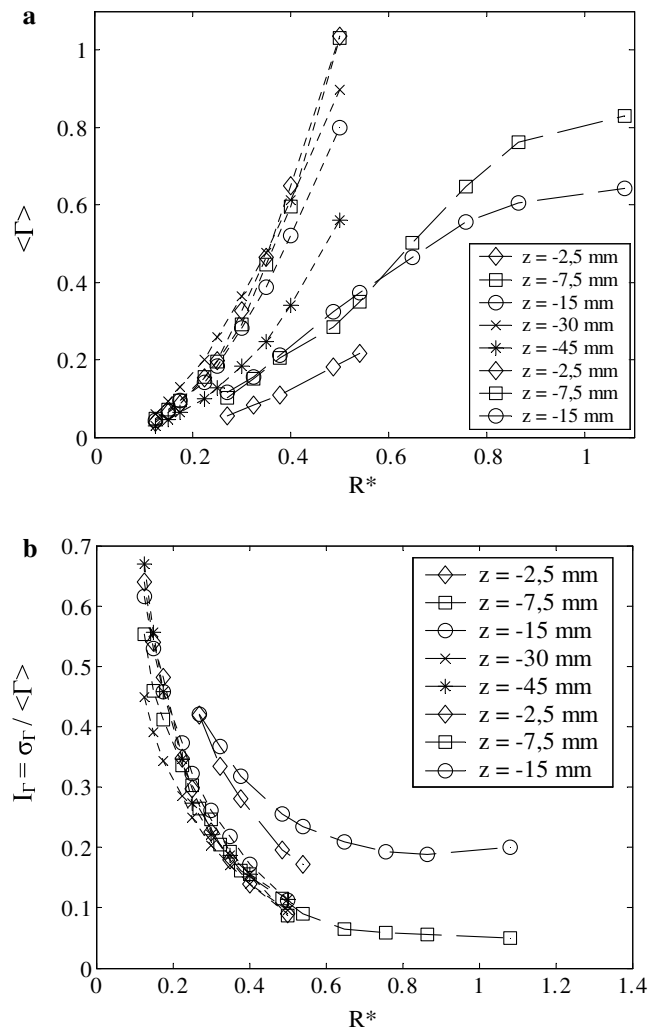
Fig. 21 Normalized circulation and fluctuation intensity as a function of a normalized radius R^*, for both cylinder [$\theta = 270$ CAD] (*short dashed line*) and in-bowl [$\theta = 360$ CAD] (*long dashed line*) measurement planes. **a** $\langle \Gamma \rangle$, **b** I_Γ

6 Appendix: list of symbols

6.1 Experimental set-up

θ	crank angle position
x	axis between the two intake ports
z	ascendant axis
S	stroke
$\bar{V}_p$	mean piston velocity
V_p	instantaneous piston velocity
ω	rotation rate of the engine
b	cylinder bore
p	depth of the bowl
d_b	diameter of the bowl
z_p	position of the piston crown
ρ	air density inside the chamber

6.2 Measurements

Δ	size of the PIV interrogation window
$\langle\ \rangle$	phase-averaging operator
M	number of velocity fields per phase
v_t	turbulent diffusivity
l	integral length scale
δ	characteristic length affected by the turbulent diffusion of momentum
t	time taken by the piston to move half way
u'	rms velocity
ρ_p	particles density
d_p	particles median diameter
μ_a	air viscosity inside the chamber
ω_S	equivalent air rotation rate
N_S	swirl number
L	size of the energy containing eddies
τ_e	engine time scale
τ_p	particles time response
τ_S	swirl time scale
τ_t	turbulent turn-over time scale
τ_Δ	turn-over time scale of eddies of the size Δ
S_t	Stokes number

6.3 Physical analysis

U	instantaneous velocity component along x axis
V	instantaneous velocity component along y axis
W	instantaneous velocity component along z axis
U_m	highest velocity magnitude
W_0	solenoidal velocity component
W_1	velocity component induced by dilatation rate
$\tilde{W}_0$	spatial average of W_0
α	angle between W and U components
Γ	circulation
Γ'	centered circulation
A	centered and reduced circulation

σ_Γ	standard deviation of the circulation
γ	contour used in the computation of the circulation
R	radius of the circle γ
β	length of the radius of γ
I_Γ	fluctuation intensity of the circulation
I	normalized correlation coefficient
i	cycle number
δI	statistical uncertainty of I
I_N	intercorrelation between cycles
N	cycle shift
$\mathbf{U_n}$	realization of the flow number (n) of the velocity vector field
$\mathbf{u_n}$	fluctuating part number (n) of $\mathbf{U_n}$
$\Phi^{(k)}$	POD mode number (k)
$\lambda^{(k)}$	POD eigenvalue number (k)
$a_n^{(k)}$	POD coefficient for the realization number (n) and the mode number (k)
$(\cdot, \cdot)$	inner product associated with the square-norm
E	total kinetic energy of the flow
m	truncation order of the POD decomposition
σ_1	standard deviation of the first POD coefficient
I_1	fluctuation intensity of the first POD coefficient
Γ_n	circulation of the realization of the flow number (n)
Γ'_n	centered circulation number (n)
$b_n^{(k)}$	normalized POD coefficients
$P^{(k)}$	correlation coefficient between normalized circulations and POD coefficients
$R*$	normalized radius

References

Arcoumanis C, Whitelaw JH (1987) Fluid mechanics of internal combustion engines—a review. IMechE 201:57–74

Arcoumanis C, Bicen AF, Whitelaw JH (1983) Squish and swirl–squish interaction in motored model engines. J Fluids Eng 105:105–112

Arcoumanis C, Hadjiapostolou A, Whitelaw JH (1987) Swirl centre precession in engine flows. SAE-Paper 870370

Arcoumanis C, Enotiadis AC, Whitelaw JH (1991) Frequency analysis of tumble and swirl in motored engines. IMechE 205:177–184

Baby X (2000) Contribution à l'optimisation de l'aérodynamique interne dans un moteur à injection directe essence. Analyse de l'écoulement de tumble par vélocimétrie par image de particules et simulation numérique 3D. PhD Thesis, I.N.P Toulouse

Batchelor G (1967) Introduction to fluid mechanics. Cambridge University Press, Cambridge

Benedict LH, Gould RD (1996) Towards better uncertainty estimates for turbulence statistics. Exp Fluids 22:129–136

Berkooz G, Holmes P, Lumley JL (1993) The proper orthogonal decomposition in the analysis of turbulent flows. Annu Rev Fluid Mech 25:539–575

Bonnet JP, Delville J, Glauser MN (2002) Coherent structures in turbulent shear flows: the confluence of experimental and numerical approaches. In: Proceedings of ASME Fluids Engineering division summer meeting. Montreal, Quebec, July 14–18. FEDSM2002–31412

Bradshaw P (1969) The analogy between streamline curvature and buoyancy in turbulent shear flow. J Fluid Mech 36:177–191

Crnojevic C, Decool F, Florent P (1999) Swirl measurements in a motor cylinder. Exp Fluids 26:542–548

Deslandes W (2004) Structure et dispersion de l'aérodynamique interne des moteurs Diesel. Caractérisation par diagnostic optique. PhD Thesis, I.N.P. Toulouse

Enotiadis AC, Vafidis C, Whitelaw JH (1990). Interpretation of cyclic flow variations in motored internal combustion engines. Exp Fluids 10:77–86

Fansler TD, French DT (1987) Swirl, Squish and Turbulence in stratified charge engines: laser-velocimetry measurements and implications for combustion. SAE-Paper 870371

Fansler TD, French DT (1988) Cycle-resolved laser-velocimetry measurements in a reentrant bowl-in-piston-engine. SAE-Paper 880377

Gerber A, Melinand JP, Charnay G (1981) Kinematic properties in a cylinder of a motored reciprocating engine. IUTAM symposium unsteady turbulent shear flows, pp 46–54

Gerber A, Charnay G, Bidault M (1985) Comparison between steady and unsteady flows in cylinders of an internal combustion engine. SAE-Paper 850121

Graftieaux L, Michard M, Grosjean N (2001) Combining PIV, POD and vortex identification algorithms for the study of unsteady turbulent swirling flows. Meas Sci Technol 12:1422–1429

Heywood JB (1988) Internal combustion engine fundamentals. McGraw-Hill, New York

Hill PG, Zhang D (1994) The effects of swirl and tumble on combustion in spark-ignition engines. Prog Energy Combust Sci 20:373–429

Lecordier B (1997) Etude de l'interaction de la propagation d'une flamme prémélangée avec le champ aérodynamique par association de la tomographie laser et de la vélocimétrie par image de particules. PhD Thesis, Faculté des Sciences de l'Université de Rouen

Lumley JL (1967) The structure of inhomogeneous turbulence. In: Yaglom A, Tatarski V (eds) Proceedings atmospheric turbulence and radio-wave propagation. Nauka, Moskow, pp 166–178

Lumley JL (1999) Engines, an introduction. Cambridge University Press, Cambridge

Payri F, Desantes JM, Pastor JV (1996). LDV Measurements of the flow inside the combustion chamber of a 4-valve D.I. diesel engine with axisymmetric piston bowls. Exp Fluids 22:118–128

Reuss DL, Adrian RJ, Landreth CC, French DT, Fansler TD (1989) Instantaneous planar measurements of velocity and large-scale vorticity and strain rate in an engine using particle image velocimetry. SAE technical papers 890616

Sirovich L (1987) Turbulence and the dynamics of coherent structures, part I: coherent structures. quarterly of applied mathematics 45–3:561–571

Tennekes H, Lumley JL (1972) A first course in turbulence. The MIT Press, Cambridge

Towers DP, Towers CE (2004) Cyclic variability measurements of in-cylinder engine flows using high-speed particle image velocimetry. Meas Sci Technol 15:1917–1925

Westerweel J (1993) Digital particle image velocimetry, theory and application. Delft University Press, Delft